

# Chapter 6

## Electrical Modelling

This chapter describes the electrical modelling done throughout the thesis. As a first approach, a simple electrical model proposed by Evans [74] was developed. It is an empirical model for estimating  $P_{MPP}$ . The development and some applications are discussed in Section 6.1. The empirical model failed to adequately reproduce certain system behaviours, such as under heterogeneous illumination conditions (e.g. during shading or isolated concentration zones). For this reason, LTSpice was used for developing a more precise electrical model, capable of reproducing entire  $I-V$  curves. This electrical model is further discussed in Section 6.2.

### 6.1 Empirical Electrical Model

This section describes the state of art, and the development of the empirical electrical model.

#### 6.1.1 State of the Art

When modelling the performance of PV modules and arrays, many simple empirical equations exist for estimating the conversion efficiency at the maximum power point ( $MPP$ ) as a function of environmental variables (e.g. in-plane irradiance, cell operating temperature, wind speed, etc.). The corresponding power output (assumed to operate at the  $MPP$ ) is obtained by multiplying the instantaneous efficiency by the total irradiance:

$$P_{MPP} = \eta \times I \times A \quad (6.1)$$

where  $\eta$  is the instantaneous efficiency,  $I$  is the global in-plane irradiance, and  $A$  is the effective solar cell surface area.

Empirical equations are widely used in the industry to estimate the annual array yield. A good review of such equations is given by Skoplaki and Palyvos [128].

For example, a simple yet powerful efficiency correlation is proposed by Evans [74]:

$$\eta = \eta_{T_{ref}} [1 + \beta(T_{cell} - T_{ref}) + \gamma \log_{10} \frac{I}{I_{ref}}] \quad (6.2)$$

where  $\eta$  is the conversion efficiency at arbitrary values of cell temperature,  $T_{cell}$  in °C, and in-plane irradiance,  $I$  in kW/m<sup>2</sup>;  $\eta_{T_{ref}}$  is the conversion efficiency at the reference values of cell temperature and in-plane irradiance ( $T_{ref} = 25$  °C,  $I_{ref} = 1$  kW/m<sup>2</sup>);  $\beta$  is the temperature coefficient (usually negative, in °C<sup>-1</sup>); and  $\gamma$  is the solar radiation coefficient, used to describe the drop of efficiency at low irradiations.

Other authors attempt to predict the cell temperature as a function of atmospheric variables such as wind speed. For example, CEA [129] proposes the following efficiency correlation:

$$\eta = 0.94 - 0.0043 \left[ \overline{T_a} + \frac{\overline{G_T}}{22.4 + 8.7\overline{V_w}} - 25 \right] \pm 2.6\% \quad (6.3)$$

where  $\eta$  is the conversion efficiency,  $\overline{T_a}$  is the daily average air temperature in °C,  $\overline{G_T}$  is the total Wh/m<sup>2</sup> received divided by the day length in h, and  $\overline{V_w}$  is the daily average wind speed.

Due to their simplicity, certain effects are not accurately taken into account. For example, complex recombination behaviours, such as intrinsic layer recombination in *a*-Si:H cells, are hard to predict. Also, string mismatch due to heterogeneous illumination of PV cells within a module (such as shadows or concentration zones) will not be reproduced. Similarly, behaviour of cells and modules under eventual reverse bias cannot be reproduced. The behaviour of by-pass diodes and their eventual influence on the electricity production cannot be represented. Finally, spectral mismatch effects resulting from the solar spectrum being different from the reference solar spectrum AM 1.5, is often not taken into account.

### 6.1.2 Implementation

Despite the simplicity and potential drawbacks of empirical electrical models, they can be useful as a basis for comparison for validating more complex models. The model proposed by Evans [74] described in Section 6.1.1 was chosen to be developed and tested for applicability to our problem. The Evans model has the advantage of being simple to implement, and that it can be applied to both *a*-Si:H and *p*-Si modules in its original form. To demonstrate the sensibility of the Evans model, efficiency was calculated for a range of temperature and transmitted flux values, as shown in Fig. 6-1.

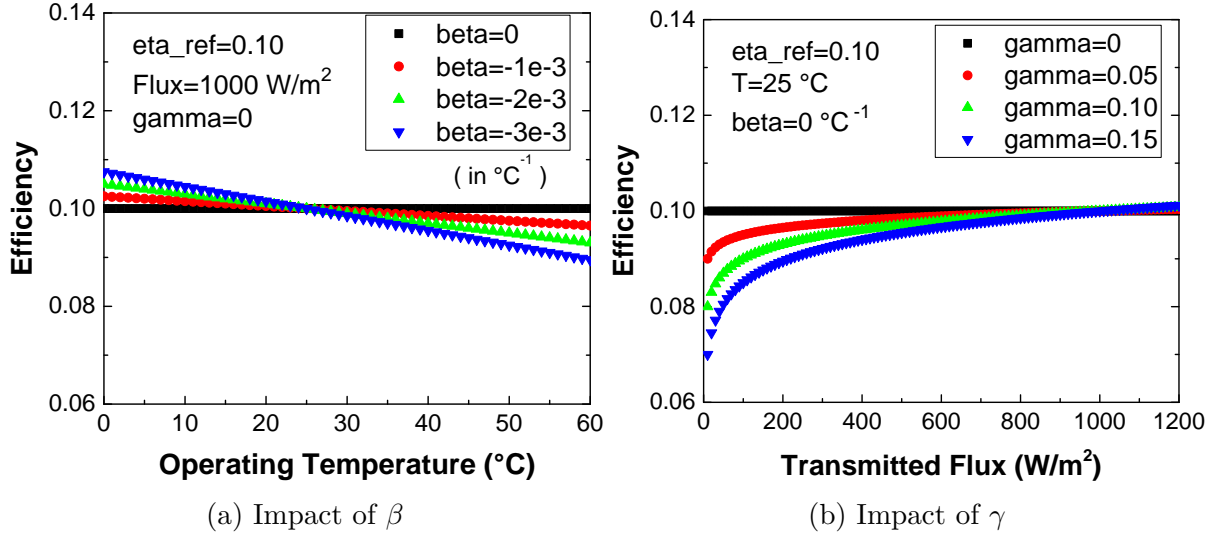


Figure 6-1: Example of the Evans model, showing its impact on the efficiency as a function of varying (a) operating temperature for several  $\beta$  values, and (b) transmitted flux for several  $\gamma$  values.

### 6.1.3 Calibration and Validation

Since flash tests were not performed on the modules in the experiment, the performance of modules under STC conditions ( $25 \text{ } ^{\circ}\text{C}$ ,  $1000 \text{ W}/\text{m}^2$ ) is unknown. For this reason, experimentally measured irradiance and operating temperature data were decided to be used for calibrating the parameters  $\eta_{\text{ref}}$ ,  $\beta$ , and  $\gamma$ .

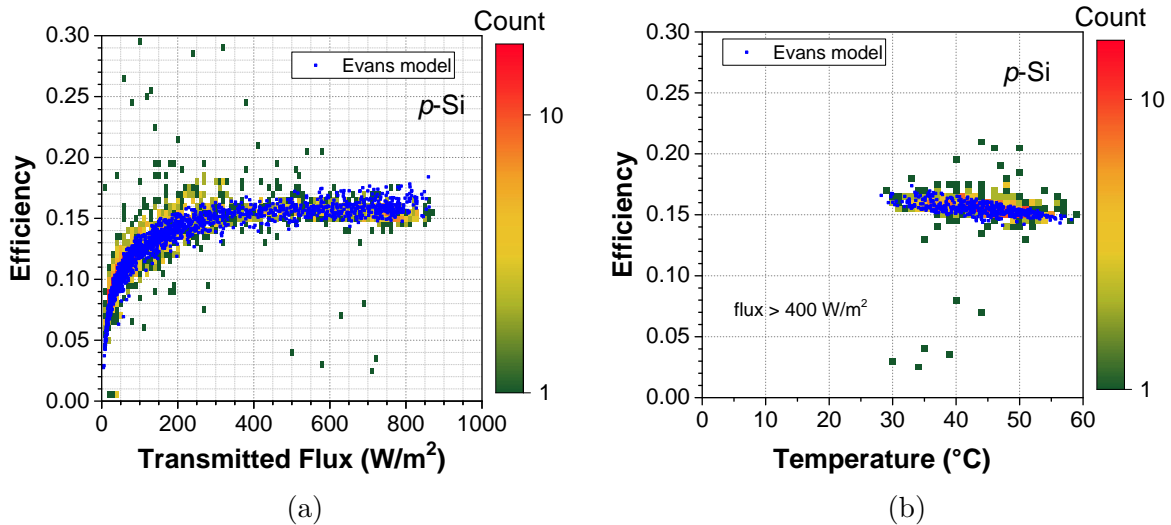


Figure 6-2: Experimental (colourbar) and numerical (by Evans, in blue) conversion efficiencies for module 5 (frontal  $p$ -Si), for the period 17th May - 6th October, 2014. Figure (a) shows the efficiency dependence on transmitted flux, while figure (b) shows the dependence on temperature (only the values corresponding to flux greater than  $400 \text{ W}/\text{m}^2$  are shown).

A simple coupled model was established as follows. The solar resource equations were

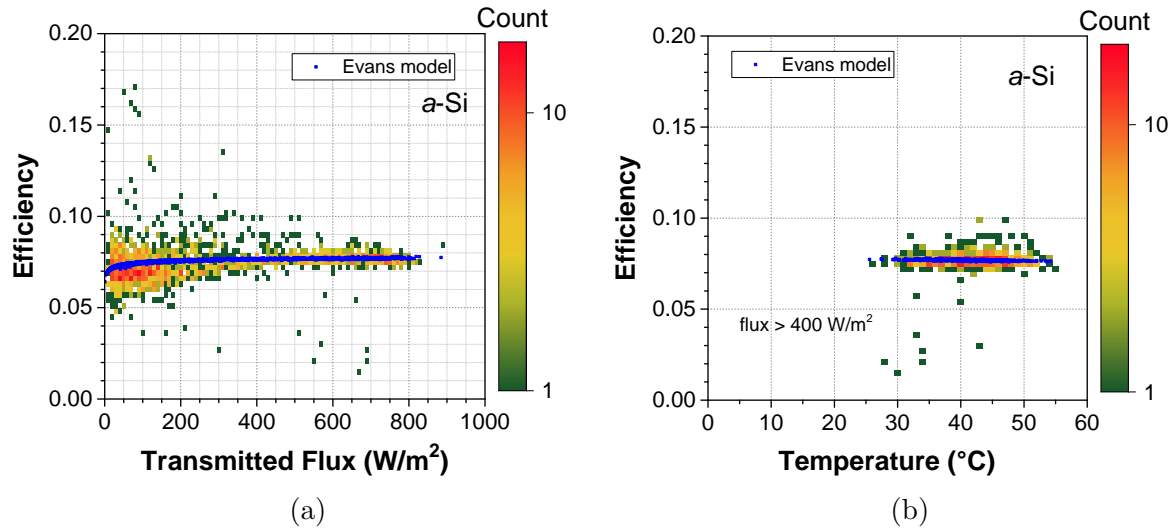


Figure 6-3: Experimental (colourbar) and numerical (by Evans, in blue) conversion efficiencies for module 6 (frontal *a*-Si:H), for the period 17th May - 6th October, 2014. Figure (a) shows the efficiency dependence on transmitted flux, while figure (b) shows the dependence on temperature (only the values corresponding to flux greater than 400 W/m<sup>2</sup> are shown).

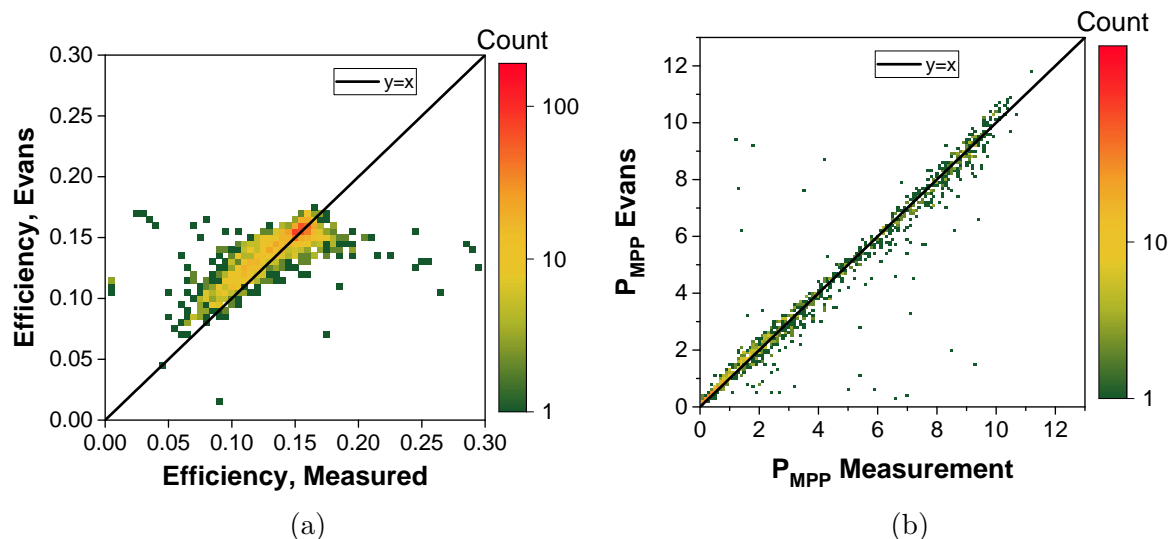


Figure 6-4: Evans model performance in predicting (a) module conversion efficiency, and (b) the  $P_{MPP}$  for module 5 (frontal  $p$ -Si) and the period 17th May - 6th October, 2014. The analytical optical model was used for calculating irradiances.

used to calculate the angle of incidence of the direct irradiance on the frontal modules of the experiment. Optical losses were calculated for the given angle of incidence. Shape factors were used to define the diffuse flux. Experimentally measured irradiance and operating temperature data were used as input to the electrical model. When needed, the operating temperature values were interpolated. Note that certain *I-V* curves were filtered out using shape-based filters and an irradiance stability filter (10% change in GHI was permitted within a preceding two-minute interval). Parameters  $\eta_{ref}$ ,  $\beta$ , and  $\gamma$

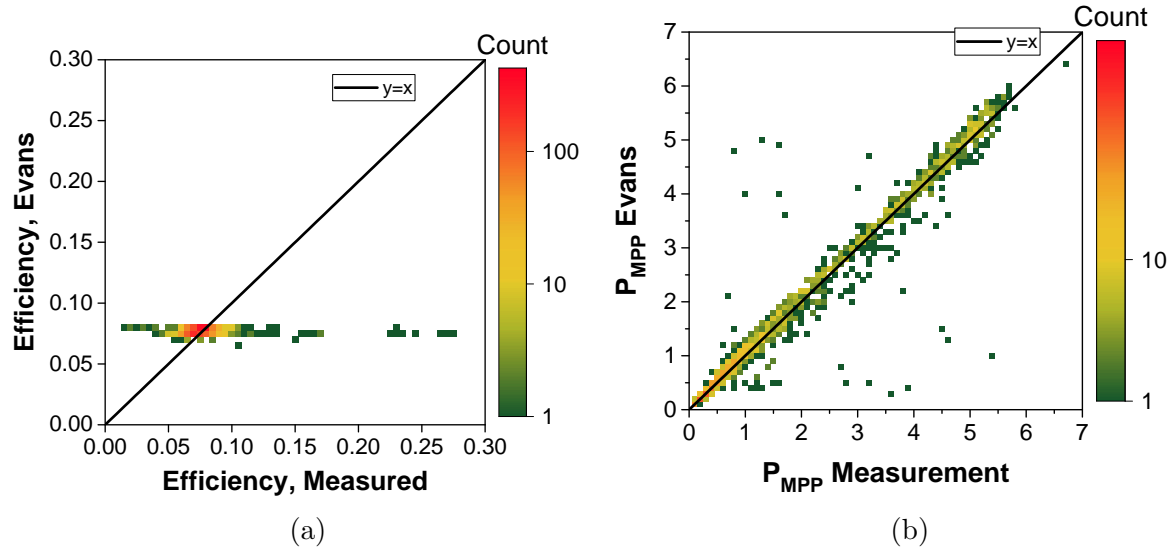


Figure 6-5: Evans model performance for predicting (a) module conversion efficiency, and (b) the  $P_{MPP}$  for module 6 (frontal  $a$ -Si:H) and the period 17th May - 6th October, 2014. The analytical optical model was used for calculating irradiances.

were varied until the modelled efficiencies matched the measured efficiencies. Note that the "measured" efficiencies still rely on some degree of modelling, for example translating horizontal to plane-of-array diffuse irradiance. The calibration results are summarised in Table 6.1.

Figures 6-2 and 6-3 show the comparison between the experimental and numerical values of efficiency for  $p$ -Si and  $a$ -Si:H modules, respectively. Comparing 6-3a and 6-2a, it is evident that  $p$ -Si modules are more sensitive to low irradiances compared to  $a$ -Si:H, experiencing higher drops in efficiency during these periods. This explains a higher value of  $\gamma$  for the  $p$ -Si case. Comparing 6-3b and 6-2b, one can note a higher sensitivity to temperature of  $p$ -Si modules compared to  $a$ -Si:H ones, explaining the difference in the values of temperature coefficients,  $\beta$ .

Figures 6-4 and 6-5 show the Evans model performance in predicting the measured efficiency and  $P_{MPP}$  values for  $p$ -Si and  $a$ -Si:H modules, respectively. In Figs. 6-5a and 6-4a one can note an occasional disagreement between experimental and modelled efficiencies. This is particularly pronounced in the case of  $a$ -Si:H, where the model predicts an almost uniform efficiency for all environmental conditions while the measured efficiency is scattered from almost 0 to almost 30%. This discrepancy is due to the previously described measurement issue during intermittent cloudy conditions, where the measured  $P_{MPP}$  values are misaligned with the assumed irradiance values, resulting in unrealistically high or low measured efficiencies. Note that in both graphs the number of points far from the diagonal is very low (marked with low bin counts, in green), while most points (marked with high bin counts, in red) lie very close to the diagonal. For this reason, a good agreement is observed between experimental and numerical values of

$P_{MPP}$ , shown in Figs. 6-4b and 6-5b.

Table 6.1: Evans parameters of  $a$ -Si:H and  $p$ -Si modules

Parameter	$p$ -Si	$a$ -Si:H
$\eta_{REF}$	0.1856	0.0793
$\beta$ ( $^{\circ}\text{C}^{-1}$ )	$-5.50 \times 10^{-3}$	$-9.54 \times 10^{-4}$
$\gamma$	0.30	0.06

## 6.2 Equivalent Circuit Electrical Model

### 6.2.1 State of the Art

Unlike the empirical models for conversion efficiency and  $P_{MPP}$  described in the previous section, such as the one proposed by Evans [74], a detailed physics-based model is necessary to explain the PV module behaviour under heterogeneous illumination of cells. In particular, the model must be able to calculate both the cell-level and module-level  $I$ - $V$  characteristics as a function of radiative and operating temperature inputs.

This section develops the notion of the equivalent circuit model, and details the final model created during this thesis.

#### 6.2.1.1 Ideal Cell Model

The simplest equivalent circuit used to model the photoelectric effect of the PV cells is the ideal cell model. It consists of a circuit with 1) a source of photogenerated current,  $I_{phot}$ , proportional to the global irradiance transmitted to the cell, and 2) a diode, representing the dark current resulting from the  $p$ - $n$  junction behaviour of the PV cell.

Figure 6-6 illustrates the resulting equivalent circuit.

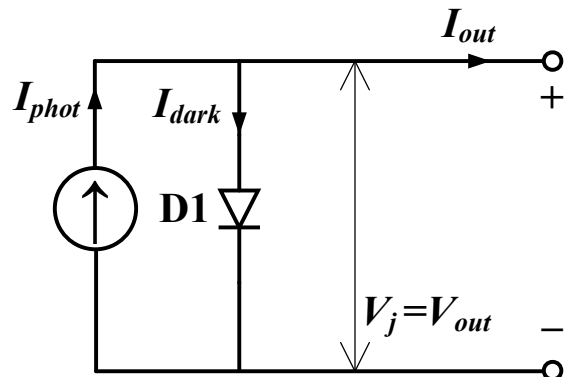


Figure 6-6: Ideal cell model consisting of a source of photogenerated current and an ideal diode ( $n = 1$ ).

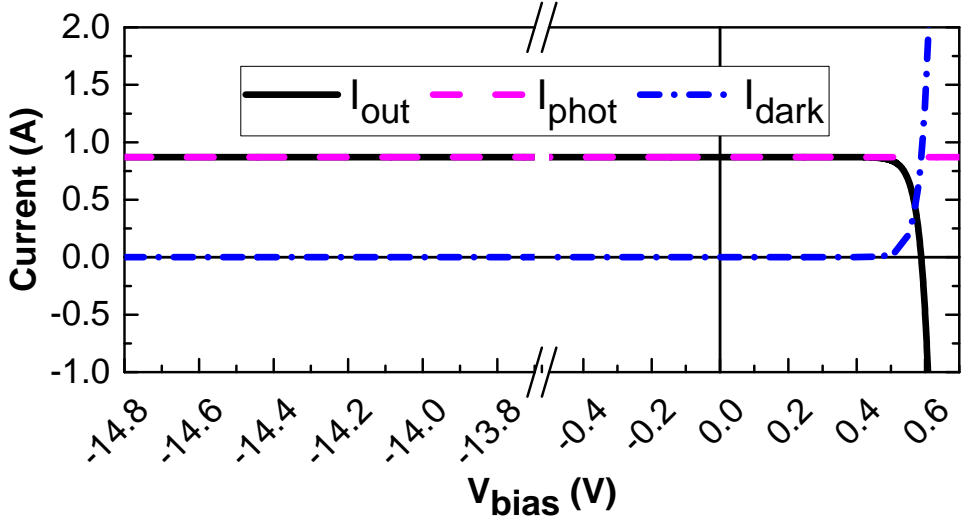


Figure 6-7: The  $I - V$  characteristics of each component of the ideal cell model circuit under STC conditions ( $T=25^\circ\text{C}$ ,  $G_{POA}=1000 \text{ W/m}^2$ ). The following parameters were used:  $I_0=9.8 \times 10^{-11} \text{ A}$ ,  $I_{SC,STC}=0.871 \text{ A}$ . The axis break is shown to demonstrate that the currents stay the same at high negative polarisations.

The circuit in Figure 6-6 results in following equation for  $I_{out}$ :

$$I_{out} = I_{phot} - I_0 \left[ \exp\left(\frac{qV_{out}}{nkT}\right) - 1 \right] \quad (6.4)$$

where  $I_{out}$  is the net current flowing through the diode in A,  $V_{out}$  is the output voltage in V,  $I_{phot}$  is the photogenerated current in A,  $I_0$  is the dark saturation current (diode leakage current in the absence of light) in A,  $q$  is the absolute value of the electron charge ( $1.602 \times 10^{-19} \text{ C}$  or  $J/V$ ),  $n$  is the diode ideality factor,  $k$  is the Boltzmann's constant ( $1.381 \times 10^{-23} \text{ J/K}$ ), and  $T$  is the diode temperature in K. The photogenerated current is generally considered as directly proportional to the incident irradiance, and calculated as follows:

$$I_{phot} = I_{SC,STC} \frac{G_{POA}}{1000 \text{ W/m}^2} \quad (6.5)$$

where  $I_{SC,STC}$  is the short circuit current at STC conditions (i.e.  $1000 \text{ W/m}^2$ ) in A and  $G_{POA}$  is the total plane-of-array irradiance in  $\text{W/m}^2$ .

To achieve a better model accuracy, an  $I_{SC}$  temperature coefficient  $\alpha$  can be added to the above definition of  $I_{phot}$  to describe the slight increase in  $I_{SC}$  with increasing operating temperature:

$$I_{phot} = I_{SC,STC} \frac{G_{POA}}{1000 \text{ W/m}^2} [1 + \alpha(T - 25^\circ\text{C})] \quad (6.6)$$

where  $\alpha$  is the  $I_{SC}$  temperature coefficient.

In the ideal case, the ideality factor,  $n$ , is set to 1. The resulting circuit is referred to

by the scientific community as the “ideal cell model”, partly because of the unity value of  $n$ , and partly because of the absence of parasitic effects described in Section 6.2.1.2. The ideal cell model is mostly used for pedagogic purposes.

Figure 6-7 shows the simulated  $I - V$  characteristics of each component of the circuit when the cell is exposed to STC conditions.

### 6.2.1.2 Single Diode Model

A more realistic model is obtained by adding resistances in series and parallel to the circuit, and using a value of  $n$  between 1 and 2 to reflect the losses due to junction recombination. The series resistance,  $R_s$ , represents the sum of series resistances at the base, emitter, metal grid, contacts and the current collecting bus. The parallel (shunt) resistance,  $R_{sh}$ , is used to reflect the leakage current due to localised shunts at the emitter layers, as well as the perimeter shunts along the cell borders. The resulting circuit is referred to by the scientific community as the “single diode model” (see Figure 6-8).

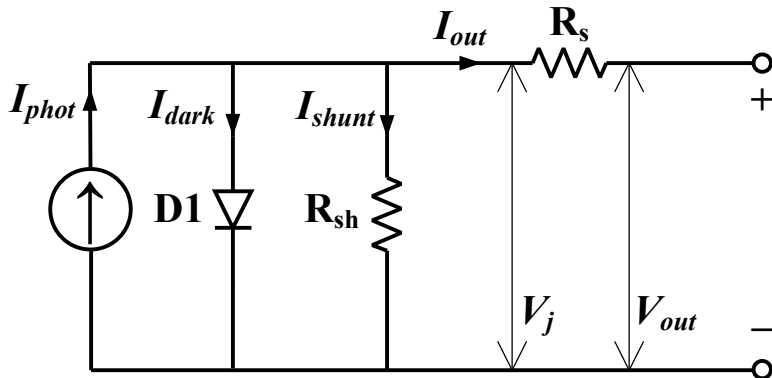


Figure 6-8: Single diode cell model consisting of a source of photogenerated current, a non-ideal diode ( $n > 1$ ), a series resistance, and a parallel (shunt) resistance.

The circuit in Figure 6-8 results in following equation for  $I_{out}$ :

$$I_{out} = I_{phot} - I_0 \left[ \exp\left(\frac{q(V_{out} + I_{out}R_s)}{nkT}\right) - 1 \right] - \frac{V_{out} + I_{out}R_s}{R_{sh}} \quad (6.7)$$

where  $I_{out}$ ,  $V_{out}$ ,  $I_{phot}$ ,  $I_0$ ,  $n$ ,  $q$ ,  $k$ , and  $T$  were defined in (6.4),  $R_s$  and  $R_{sh}$  are the cell series and shunt resistances, respectively, in  $\Omega$ .

Figure 6-9 shows the simulated  $I - V$  characteristics of each component of the circuit when the cell is exposed to STC conditions.

Note that this is the most widely used model in the industry, because it is simple and applicable to a variety of PV technologies with an acceptable accuracy. However, due to its simplicity it fails to capture several phenomena such as the recombination at the space charge region (for crystalline silicon devices), the intrinsic layer ( $i$ -layer) recombination (for amorphous silicon devices) and the junction breakdown in reverse bias conditions (for

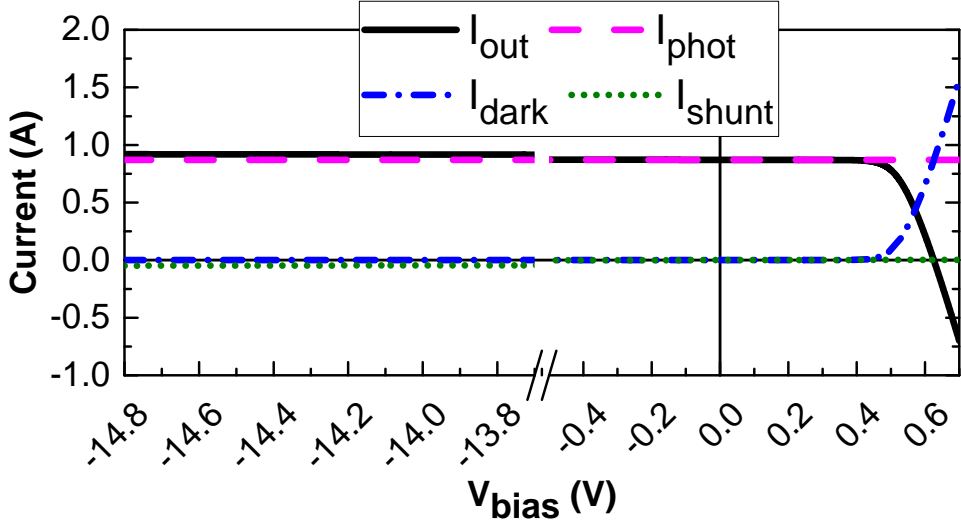


Figure 6-9: The  $I - V$  characteristics of each component of the single diode cell model circuit under STC conditions ( $T=25$  °C,  $G_{POA}=1000$  W/m<sup>2</sup>). The following parameters were used:  $I_0=9.8 \times 10^{-11}$  A,  $I_{SC,STC}=0.871$  A,  $R_{sh}=3.0 \times 10^2$  Ω,  $R_s=4.2 \times 10^{-2}$  Ω,  $n=1.000$ . The axis break is shown to demonstrate the evolution of the shunt current with voltage bias.

both crystalline and amorphous silicon devices). For this reason, this model is commonly expanded, as detailed in the next sections.

#### 6.2.1.3 Double Diode Model

The next improvement in the equivalent circuit model is to attempt to model the recombination at the space charge region, explaining the non-ohmic current paths in parallel with the intrinsic solar cell. This is often done by adding a secondary diode in parallel with the first, where the ideality factor is generally set to a value close to 2.

Figure 6-10 illustrates the resulting equivalent circuit:

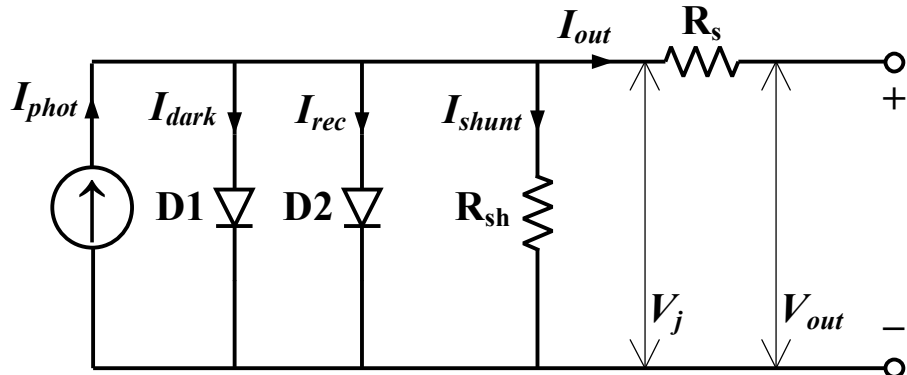


Figure 6-10: Double diode cell model consisting of a source of photogenerated current, a non-ideal diode ( $n > 1$ ), a series resistance, and a parallel (shunt) resistance.

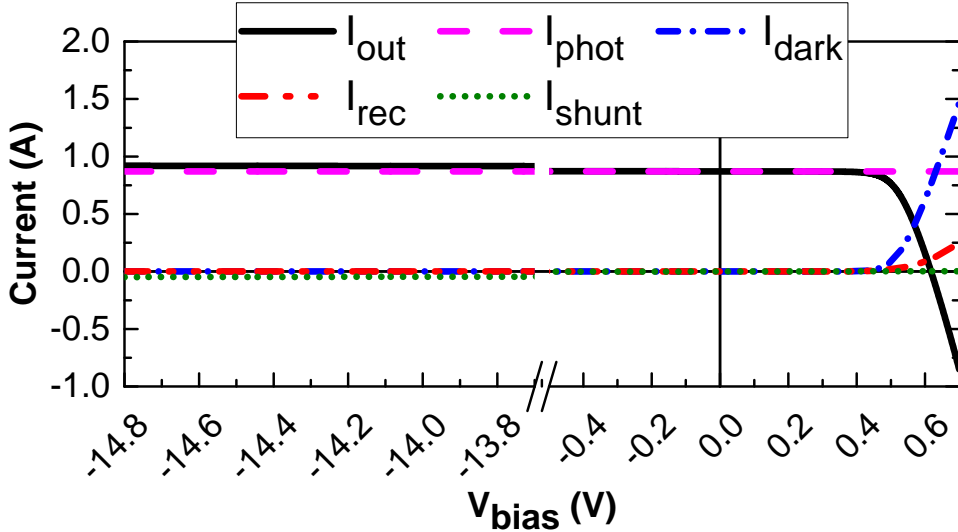


Figure 6-11: The  $I - V$  characteristics of each component of the double diode model circuit under STC conditions ( $T=25$  °C,  $G_{POA}=1000$  W/m<sup>2</sup>). The following parameters were used:  $I_{01}=9.8 \times 10^{-11}$  A,  $I_{02}=2.2 \times 10^{-7}$  A,  $I_{SC,STC}=0.871$  A,  $R_{sh}=3.0 \times 10^2$  Ω,  $R_s=4.2 \times 10^{-2}$  Ω,  $n_1=1.000$ , and  $n_2=1.819$ .

The circuit in Figure 6-10 results in following equation for  $I_{out}$ :

$$I_{out} = I_{phot} - I_{01} \left[ \exp\left(\frac{q(V_{out} + I_{out}R_s)}{n_1 kT}\right) - 1 \right] - I_{02} \left[ \exp\left(\frac{q(V_{out} + I_{out}R_s)}{n_2 kT}\right) - 1 \right] - \frac{V_{out} + I_{out}R_s}{R_{sh}} \quad (6.8)$$

where  $I_{out}$ ,  $V_{out}$ ,  $I_{phot}$ ,  $I_0$ ,  $q$ ,  $k$ ,  $T$ ,  $R_s$  and  $R_{sh}$  were defined in (6.7),  $n_1$  and  $n_2$  are the ideality factors for the two diodes, and  $I_{01}$  and  $I_{02}$  are the dark saturation currents of the two diodes in A.

Figure 6-11 shows the simulated  $I - V$  characteristics of each component of the circuit when the cell is exposed to STC conditions.

Note that  $I_{dark}$  and  $I_{rec}$  currents given by the two diodes differ in behaviour due to the different values of diode parameters ( $I_0$  and  $n$ ). The fact of having two diodes provides a much greater flexibility in fitting the experimental data with the model.

#### 6.2.1.4 *i*-Layer Recombination in Amorphous Silicon Devices

While a second diode is appropriate for modelling the space charge region recombination in crystalline silicon (c-Si) devices, a better approach exists for amorphous silicon (*a*-Si:H) devices. Since the recombination losses in *a*-Si:H devices are predominantly due to the recombination in the intrinsic layer (*i*-layer), the recombination current has a slightly

different behaviour from a diode. An approach for modelling this behaviour has been proposed by Merten et al. [130], and given in the equation below:

$$I_{rec} = I_{phot} \frac{d_i^2}{(\mu\tau)_{eff}[V_{bi} - (V_{out} + I_{out}R_s)]} \quad (6.9)$$

where  $I_{rec}$  is the  $i$ -layer recombination current in A,  $I_{phot}$  is the photogenerated current in A,  $d_i$  is the thickness of the  $i$ -layer in cm,  $(\mu\tau)_{eff}$  is the effective mobility-lifetime product in  $\text{cm}^2/\text{V}$ ,  $V_{bi}$  is the built-in voltage in V, and  $(V_{out} + I_{out}R_s)$  is the junction voltage in V.

Figure 6-12 illustrates the resulting equivalent circuit:

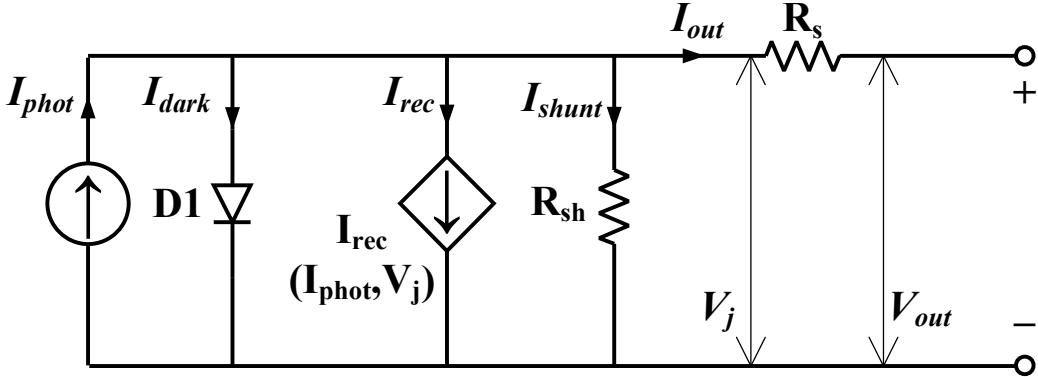


Figure 6-12: Merten cell: single diode cell model with the added Merten term represented by a current sink.

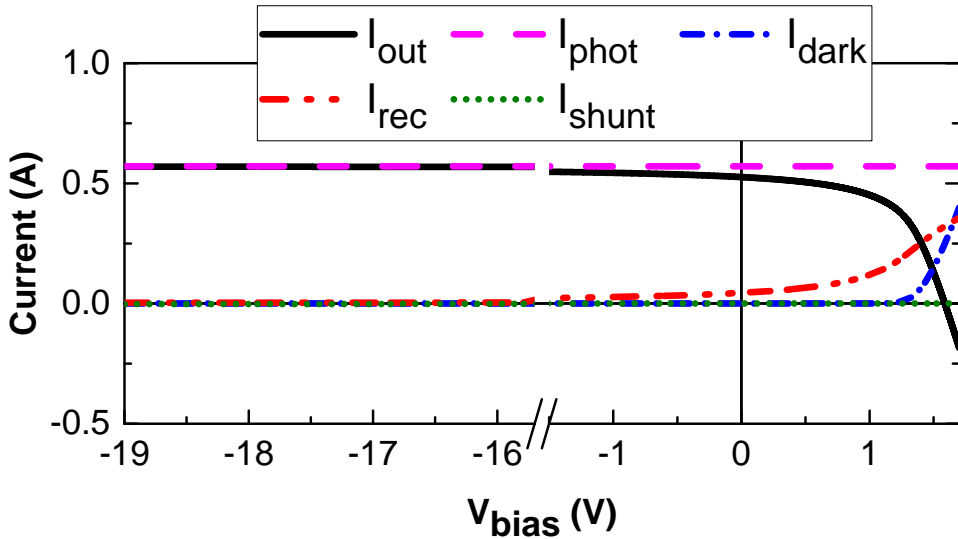


Figure 6-13: The  $I$ - $V$  characteristics of each component of the double diode model circuit under STC conditions ( $T=25^\circ\text{C}$ ,  $G_{POA}=1000 \text{ W/m}^2$ ). The following parameters were used:  $I_0=5.4 \times 10^{-17} \text{ A}$ ,  $I_{SC,STC}=0.571 \text{ A}$ ,  $R_{sh}=9.7 \times 10^3 \Omega$ ,  $R_s=5.0 \times 10^{-1} \Omega$ , and  $n=1.700$ .

Figure 6-13 shows the simulated  $I$ - $V$  characteristics of each component of the circuit when the cell is exposed to STC conditions.

### 6.2.1.5 Junction Breakdown

If a given PV cell within a string of series-connected cells is shaded (e.g. by leaves or bird droppings), it can be reverse-biased to voltages up to -15 V depending on the module architecture, and can therefore dissipate the power generated by the neighbouring cells exhibiting full illumination. This power dissipation can lead to hot spots, inducing irreversible damage to PV modules.

All  $p-n$  junction devices have a certain value of reverse bias, called breakdown voltage,  $V_{br}$ , at which the junction "breaks down" and lets an enormous amount of current pass through the junction. This can be very dangerous for the PV cell, as it can result in excessive heating and permanent damage. This value varies by cell type, and has been reported to range from -7.2 V to -25.2 V [131]. The design of PV modules must take this into account, so that under the worst case of cell reverse bias (e.g. under extreme partial shading of a cell during high irradiances), the cell is not reverse-biased beyond its respective  $V_{br}$ . For this reason, bypass diodes are often added to reduce the maximum cell reverse bias under the worst-case scenario, and hence avoid a junction breakdown.

To model this behaviour one can follow the procedure outlined by Bishop [132]. The standard single- and double-diode models describe the leakage current by a parallel resistance, where the current is defined as the junction voltage divided by resistance value. Bishop recommends to modify this term to describe the voltage breakdown:

$$I_{br} = \frac{V_{out} + I_{out}R_s}{R_{sh}} \left[ a \left( 1 - \frac{V_{out} + I_{out}R_s}{V_{br}} \right)^{-m} \right] \quad (6.10)$$

where  $I_{br}$  is the leakage current in the cell reverse characteristic in A,  $(V_{out} + I_{out}R_s)$  is the voltage across the junction in V,  $R_{sh}$  is the cell shunt resistance in  $\Omega$ ,  $a$  is the fraction of ohmic current involved in avalanche breakdown, and  $m$  is the avalanche breakdown exponent. The resulting term is a function of junction voltage  $(V_{out} + I_{out}R_s)$  and controls the cell reverse characteristic.

The total leakage current becomes:

$$I_{shunt} = \frac{V_{out} + I_{out}R_s}{R_{sh}} \left[ 1 + a \left( 1 - \frac{V_{out} + I_{out}R_s}{V_{br}} \right)^{-m} \right] \quad (6.11)$$

Figure 6-14 illustrates the resulting equivalent circuit.

Figure 6-15 shows the simulated  $I-V$  characteristics of each component of the circuit when the cell is exposed to STC conditions.

## 6.2.2 Implementation

This section details the implementation of the electrical model for the PV modules of two technologies:  $a\text{-Si:H}$  and  $p\text{-Si}$ . The strategy is to first model the behaviour of individual

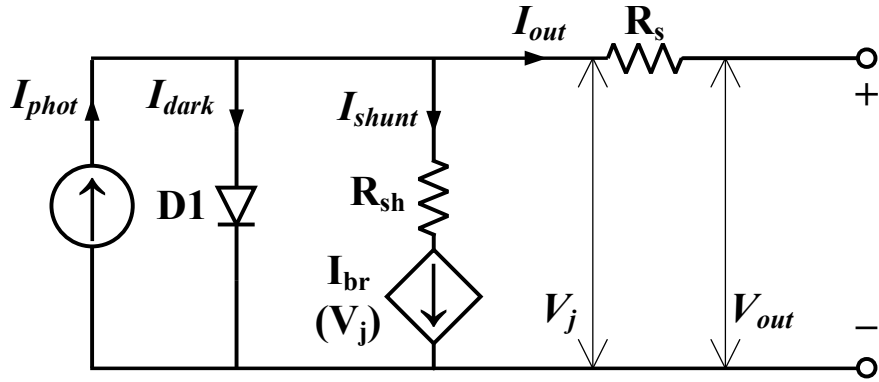


Figure 6-14: Bishop cell: single diode cell model with the added Bishop term represented by a current sink.

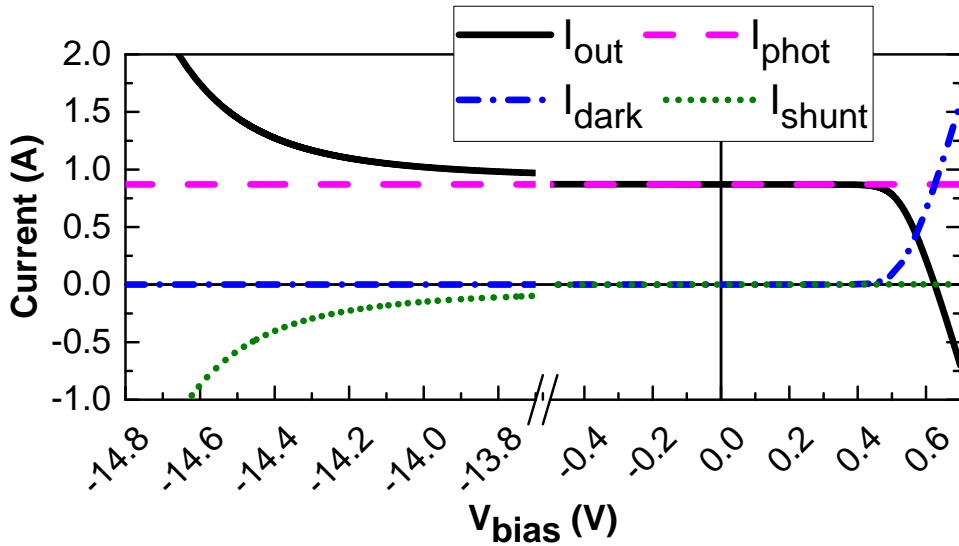


Figure 6-15: The  $I$ - $V$  characteristics of each component of the Bishop cell model circuit under STC conditions ( $T=25$  °C,  $G_{POA}=1000$  W/m<sup>2</sup>). The following parameters were used:  $I_0=9.8 \times 10^{-11}$  A,  $I_{SC,STC}=0.871$  A,  $R_{sh}=3.0 \times 10^2$  Ω,  $R_s=4.2 \times 10^{-2}$  Ω,  $n=1$ ,  $a=2.4 \times 10^{-3}$ ,  $V_{br}=15$  V,  $m=2.57$ .

cells, and then connect them accordingly. Note that the equations used to describe the output current as a function of voltage bias are transcendental, necessitating an iterative approach for their resolution. This is luckily a built-in feature in most SPICE implementations. In the case of LTSpice, the Newton-Rapson method is implemented.

### 6.2.2.1 Modelling of PV Cells

Two different electrical circuits are proposed for describing the behaviour of individual *a*-Si:H and *p*-Si cells, respectively (see Figs. 6-16 and 6-17).

For the *a*-Si:H cell (Figure 6-16), a single-diode model is proposed with the addition of the Merten ( $I_{rec}$ ) and Bishop ( $I_{br}$ ) terms. For the *p*-Si cell (Figure 6-17), a double-diode model is proposed with the addition of the Bishop ( $I_{br}$ ) term. In both cases, the slight increase in short circuit current with temperature was introduced in the photogenerated

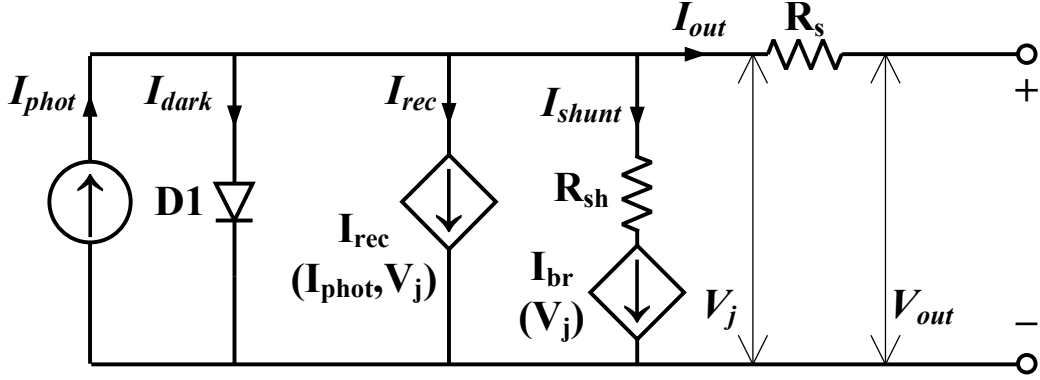


Figure 6-16: *a*-Si:H cell: single diode cell model with the added Bishop and Merten terms, both represented by current sinks.

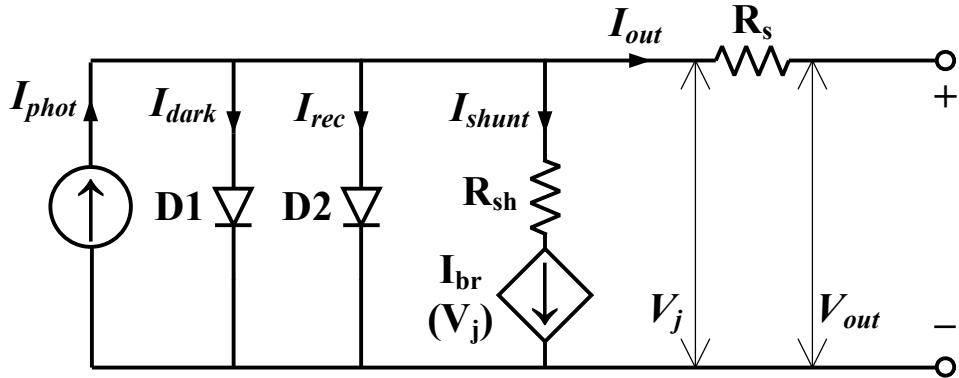


Figure 6-17: *p*-Si cell: double diode cell model with the added Bishop term represented by a current sink.

current source term. The following equations describe the *a*-Si:H circuit:

$$\begin{aligned}
 I_{out,a-Si:H} = & I_{SC,STC} \frac{G_{POA}}{1000W/m^2} [1 + \alpha(T - 25^\circ C)] \\
 & - I_{01} \left[ \exp \left( \frac{q(V_{out} + I_{out}R_s)}{n_1 k T} \right) - 1 \right] \\
 & - I_{phot} \frac{d_i^2}{(\mu\tau)_{eff} [V_{bi} - (V_{out} + I_{out}R_s)]} \\
 & - \frac{V_{out} + I_{out}R_s}{R_{sh}} \left[ 1 + a \left( 1 - \frac{V_{out} + I_{out}R_s}{V_{br}} \right)^{-m} \right]
 \end{aligned} \tag{6.12}$$

or equivalently

$$\begin{aligned}
 I_{out,a-Si:H} = & I_{SC,STC} \frac{G_{POA}}{1000W/m^2} [1 + \alpha(T - 25^\circ C)] \left\{ 1 - \frac{d_i^2}{(\mu\tau)_{eff} [V_{bi} - (V_{out} + I_{out}R_s)]} \right\} \\
 & - I_{01} \left[ \exp \left( \frac{q(V_{out} + I_{out}R_s)}{n_1 k T} \right) - 1 \right] \\
 & - \frac{V_{out} + I_{out}R_s}{R_{sh}} \left[ 1 + a \left( 1 - \frac{V_{out} + I_{out}R_s}{V_{br}} \right)^{-m} \right]
 \end{aligned} \tag{6.13}$$

Similarly to *a*-Si:H, the following equation describes the *I-V* characteristic of the *p*-Si circuit:

$$\begin{aligned}
 I_{out,p-Si} = & I_{SC,STC} \frac{G_{POA}}{1000W/m^2} [1 + \alpha(T - 25^\circ C)] \\
 & - I_{01} \left[ \exp \left( \frac{q(V_{out} + I_{out}R_s)}{n_1 kT} \right) - 1 \right] \\
 & - I_{02} \left[ \exp \left( \frac{q(V_{out} + I_{out}R_s)}{n_2 kT} \right) - 1 \right] \\
 & - \frac{V_{out} + I_{out}R_s}{R_{sh}} \left[ 1 + a \left( 1 - \frac{V_{out} + I_{out}R_s}{V_{br}} \right)^{-m} \right]
 \end{aligned} \tag{6.14}$$

where  $I_{SC,STC}$  is the short circuit current at STC conditions in A,  $G_{POA}$  is the plane-of-array irradiance in  $W/m^2$ ,  $\alpha$  is the  $I_{SC}$  temperature coefficient, and the rest of the terms were defined previously.

Using LTSpice, the two circuits were exposed to STC conditions, and the *I-V* characteristics of different circuit components were extracted (see Figs. 6-18 and 6-19).

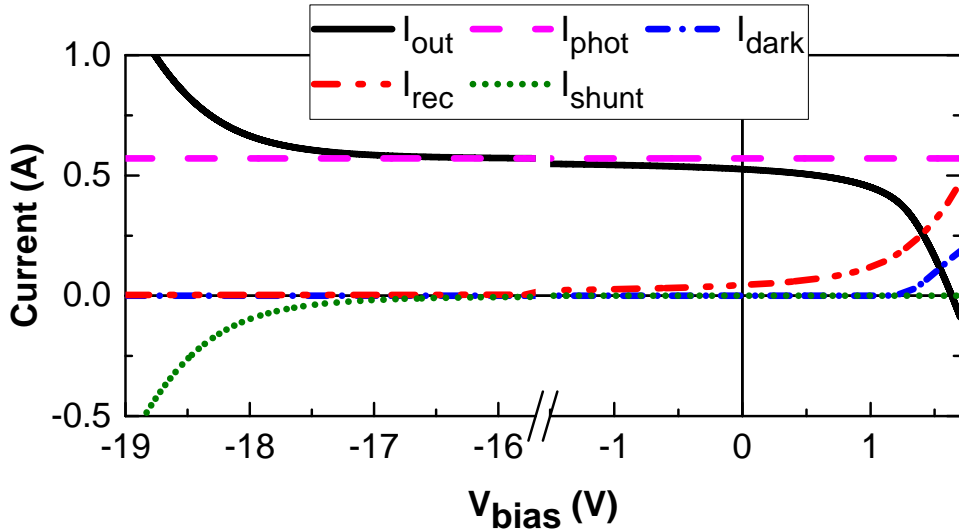


Figure 6-18: Current in each component of the proposed *a*-Si:H cell model as a function of the applied voltage bias. The cell was parametrised using the values shown in Table 7.1 and subjected to STC conditions.

Figure 6-18 shows the current in each component of the *a*-Si:H cell equivalent circuit.  $I_{out}$  (shown in black) is the output current of the cell, and is equal to  $I_{phot} - I_{dark} - I_{rec} - I_{shunt}$ . The photogenerated current (shown in pink), is constant for all values of voltage bias, and is proportional to the total incident flux on the cell. It is set to increase slightly with temperature, according to (6.6). Since STC is applied,  $I_{phot}$  is equal to  $I_{SC,STC}$  (0.57 A).  $I_{dark}$ , the dark saturation current (shown in blue), follows the typical behaviour of a diode, having zero current for negative and slightly positive values of voltage bias, and rising exponentially for voltage bias values greater than the diode built-in voltage

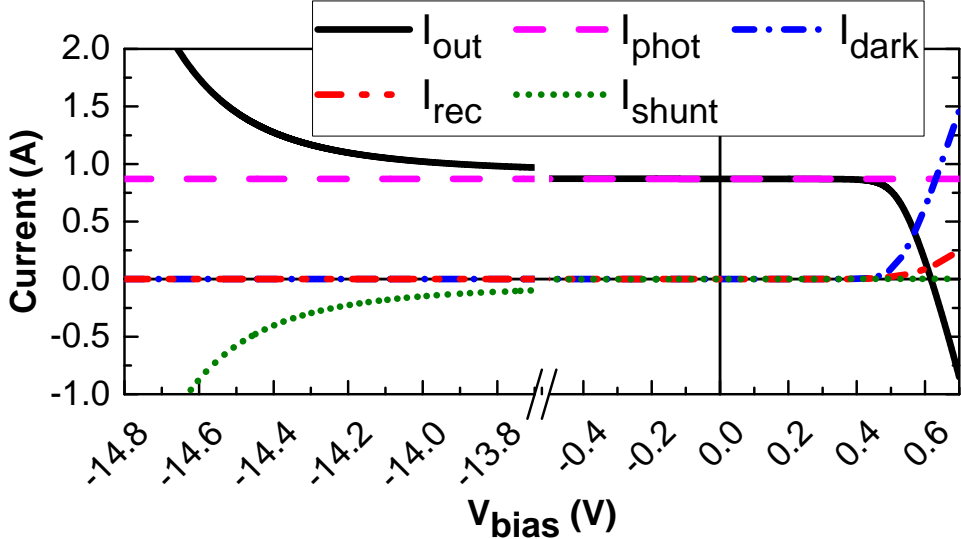


Figure 6-19: Current in each component of the proposed *p*-Si cell model as a function of the applied voltage bias. The cell was parametrised using the values shown in Table 7.1 and subjected to STC conditions.

( $V_{bi}$ ). Typical silicon diodes have a  $V_{bi}$  of about 0.7 V. However, as seen in the figure the *a*-Si:H cell was found to have a  $V_{bi}$  greater than 1 V. This is because the cells within the experimental modules are in fact tandem cells composed of two sub-cells stacked vertically. The effective  $V_{bi}$  therefore represents the total  $V_{bi}$  of the two sub-cells. In this figure and in further modelling, an *a*-Si:H cell refers to a tandem cell, while an *a*-Si:H module is considered to have 14 cells connected in series (even though the module specification indicates there are 28 cells in total).  $I_{rec}$ , the *i*-layer recombination current (shown in red), reflects the use of the equation proposed by Merten et al. [130]. Compared with the diode equation, 1) it converges to a small non-zero value as  $V_{bias}$  tends to  $-\infty$  V, 2) at  $V_{bias}=0$  V, significant recombination current is observed, 3) it is much higher in amplitude in the region  $[0, V_{OC}]$ , and 4) has a different shape. As seen in the figure, this term is the dominant loss mechanism.  $I_{shunt}$ , the shunt current (shown in green), increases gradually with  $V_{bias}$  for positive bias values. The slope of the increase depends on the value of  $R_{sh}$ . The current is 0 A at  $V_{bias}=0$  V and for slightly negative values of  $V_{bias}$ . As  $V_{bias}$  approaches the set breakdown voltage of -20 V,  $I_{shunt}$  increases rapidly in the negative direction, letting an enormous amount of current pass through the cell.

Figure 6-19 shows the current in each component of the *p*-Si cell equivalent circuit. Similarly to the *a*-Si:H cell, the  $I_{phot}$  is constant throughout the range of the  $V_{bias}$  sweep. As STC conditions were simulated,  $I_{phot}=I_{SC,STC}=0.87$  A.  $I_{dark}$  (in blue) and  $I_{rec}$  (in red) follow diode equations with different sets of parameters, yielding a dark current which is much higher than the recombination current. It is observable that the  $V_{bi}$  of both diodes is around 0.7 V, as expected. Finally,  $I_{shunt}$  behaves similarly to the case of *a*-Si:H cells, rising gradually during positive values of  $V_{bias}$ , and increasing rapidly in the negative

direction as  $V_{bias}$  approaches the breakdown voltage of -15 V.

### 6.2.2.2 Modelling of PV Modules

After having developed the model of the electrical behaviour of a cell, the next step was to model the behaviour of entire modules. PV modules most commonly consist of PV cells connected in series, with the goal of maximising the open circuit voltage of the module. For example, the *a*-Si:H modules installed in the experiment consist of 14 tandem cells connected in series, while the *p*-Si module consists of 36 cells connected in series (see Figs. 3-10a and 3-10b, page 35). In the case of *p*-Si modules with a large number of cells connected in series, bypass diodes are often added across a certain number of the cells, which are referred to as being in a string. The goal of bypass diodes is to provide an alternate path for current flow during certain configurations of current mismatch, such as during partial shading conditions. The *p*-Si module in the experiment consists of 36 cells in series and two bypass diodes across each of the strings of 18 cells. Bypass diodes are generally not added to *a*-Si:H modules, even if there are many cells connected in series. The main reason for this is that *a*-Si:H cells are generally long (spanning the entire height of the module) making the *a*-Si:H modules less susceptible to partial shading.

Several solutions exist for modelling the PV modules as series-connected cells, such as PVSIM [133], Simulink [134] and Spice [135]. Spice analog simulator was chosen as the simulation tool since it is open-source and known to have a great performance. It uses state of the art convergence methods and well-established iterative procedures to calculate the currents and voltages at any part of the circuit. Furthermore, it supports circuits of arbitrary complexities. It is being packaged into a graphical interface by several enterprises, some selling it as a product (e.g. PSpice [136]) while other releasing it for free. Two free alternatives were tested: LTSpice [137] was tested under the Microsoft Windows environment, and ngspice [138] under the Linux environment.

Circuits are defined in files .cir, which can be developed 1) by drawing the schematics using the graphical interface of the software and converting them into a .cir file, or 2) manually (e.g. using an external program). It is desirable to be able to systematically create .cir files of PV modules comprising an arbitrary number of cells and their irradiances and operating temperatures. Therefore, a C++ code has been developed to dynamically generate .cir files as a function of PV technology and module topology.

For additional flexibility and at the same time clarity of the PV module .cir file, the definition of the PV cell circuit was defined in a separate file, conventionally a .lib file. The .lib file is then included in the main .cir file, and the PV cells are easily implemented as subcircuits (see Fig. 6-20).

The C++ code connects a chosen number of PV cells in series by systematically numbering the nodes of each subcircuit (that of an individual cell) within the .cir file. It

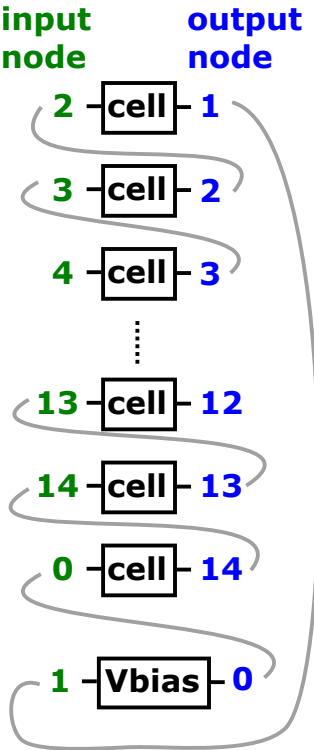


Figure 6-20: Illustration of subcircuit node numbering within the PV module .cir file for connecting PV cells in series. Example given is for a 14-cell module. The system is grounded by numbering one node with 0.

makes sure that the overall circuit is grounded (by adding node 0), and adds a voltage bias between the first and last cells (to be stepped during the simulation). It adds a chosen number of bypass diodes, in our case 0 or 2 for *a*-Si:H and *p*-Si, respectively. It writes modelled or measured irradiance and operating temperature values of each PV cell.

Finally, for the purpose of evaluating the *I-V* curve of the assembly, a DC sweep directive is added, varying the voltage bias from 0 V (short circuit conditions) to a point beyond the open circuit conditions (for example 25 V), with a step of 0.01 V.

Both LTSpice and ngspice support the batch mode, where Spice is called externally with the path of the .cir file given as an argument. In this case, the need for a graphic interface is eliminated, and more resources are available for the calculation. Furthermore, this allows one to pilot Spice calculations externally, effectively coupling the electrical model with the rest of the model. As the calculation result was to be imported by the piloting program, Spice needed to be configured to produce ASCII result files (written in .RAW files), as the default is a binary output.

### 6.2.3 Example: Partial Shading

Partial shading of a PV module (in the worst case, total shading of a single cell) can be of particular danger to its lifetime and performance, as the shaded cell can be reverse-

biased into conditions where it dissipates significant amounts of power. Power dissipation results in significant heat generation within the cell, which can lead to temporary and permanent performance degradation. It is therefore an important design factor for PV modules, and is brought to a minimum by:

- optimising the breakdown voltage of the cell junction thereby reducing the risk of avalanche breakdown, and
- introducing bypass diodes across a certain number of series-connected cells, reducing the worst-case amount of reverse bias

The SPICE electrical model has been used to study the behaviour of partially shaded modules, as described in the following two studies.

#### 6.2.3.1 Study 1: STC vs. Partial Shading

In the first study, a *p*-Si module was simulated under two scenarios:

1. STC conditions ( $1000 \text{ W/m}^2$ ,  $25^\circ\text{C}$ ) - hence uniform illumination
2. STC conditions with cell 9 shaded by 50%

Figures 6-21, 6-22, 6-23, and 6-24 illustrate cell currents, cell voltages, bypass diode currents, and bypass diode voltages, respectively, as a function of applied voltage bias for the two scenarios.

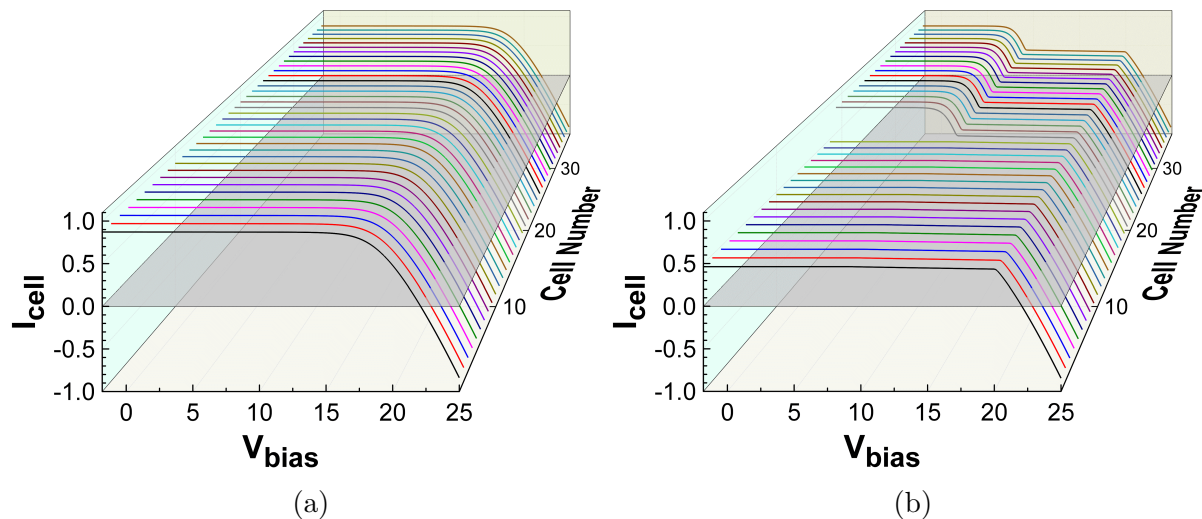


Figure 6-21: *p*-Si cell currents: (a) at STC, and (b) with cell 9 shaded by 50 %.

Under Scenario 1 (STC conditions, uniform illumination), the cell currents are the same for all 36 cells for a given voltage bias (see Fig. 6-21a). In this case they are around 0.87 A in short circuit conditions. The imposed voltage is uniformly distributed among the cells, resulting in equal voltage across each cell, and increasing linearly with the applied bias (see Fig. 6-22a). For example, if a bias of +18 V is imposed across the module, each cell operates under  $18 \text{ V} / 36 = +0.5 \text{ V}$ . Under these conditions, both strings and therefore both bypass diodes are biased to +9 V. Since the bypass diodes

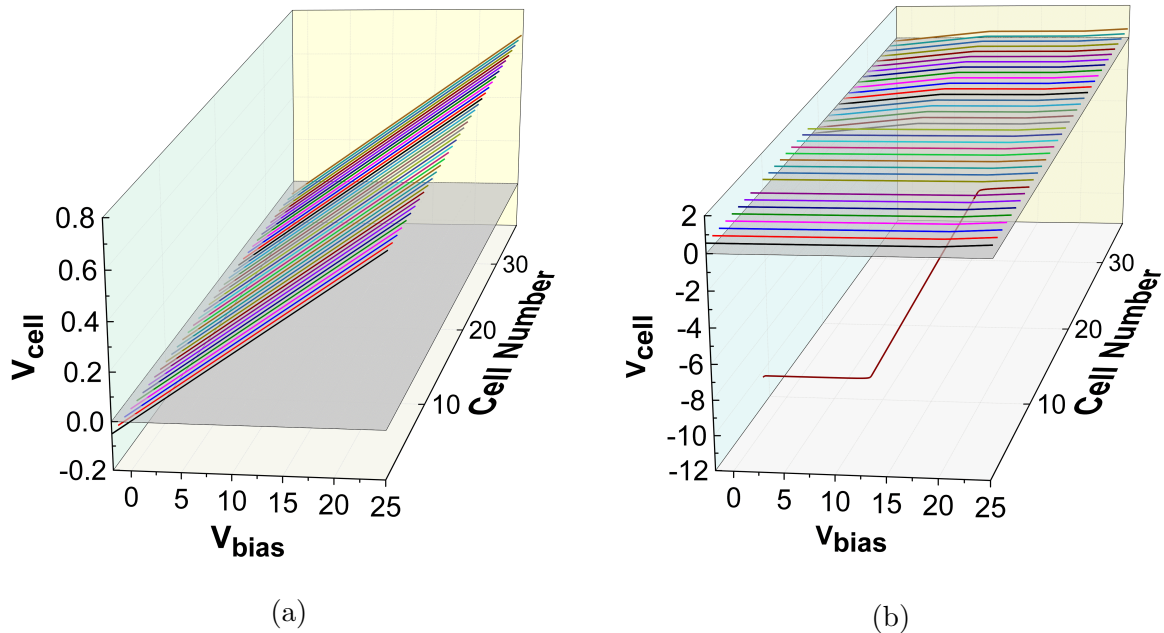


Figure 6-22: *p*-Si cell voltages: (a) at STC, and (b) with cell 9 shaded by 50 %.

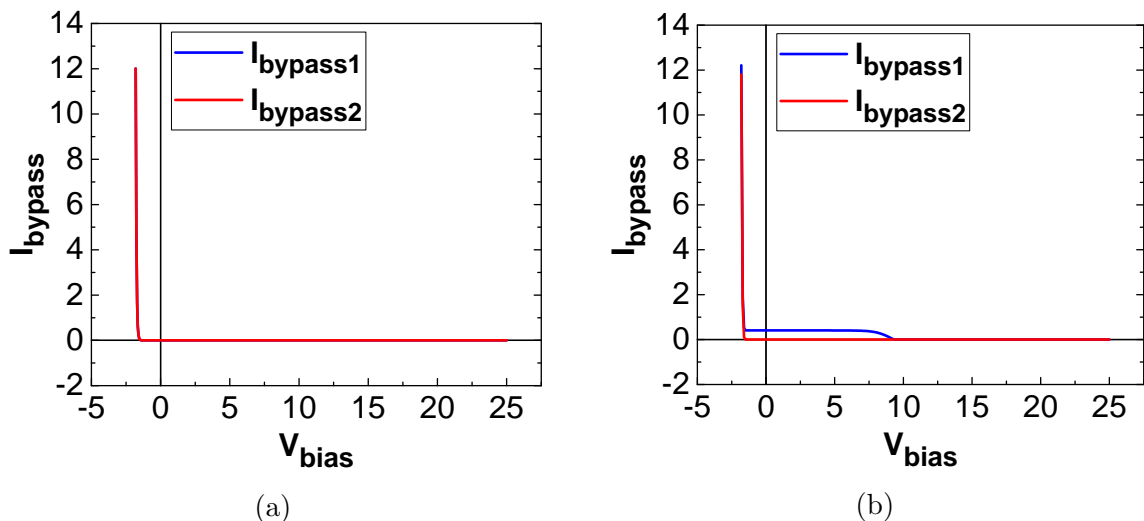


Figure 6-23:  $p$ -Si bypass diode currents: (a) at STC, and (b) with cell 9 shaded by 50 %.

only get activated in reverse bias conditions when the string voltage reaches about -0.7 V, they remain off under these conditions (see Figs. 6-23a and 6-24a).

Scenario 2 represents a partial shading condition. When a cell is partially shaded, it is the photocurrent that it is capable of generating which limits the current that flows through the string. For example, a 50% shading results in a short circuit current of 0.46 A (53% compared to unshaded case) for all cells in the affected string (see Fig. 6-21b). This limit in current imposes a constraint on the operating voltage of non-shaded cells in the affected string, ranging between around 0.56 V (corresponding to the limiting current of 0.46 A), and around 0.61 V (the cell-level open-circuit voltage) - see Fig. 6-25.

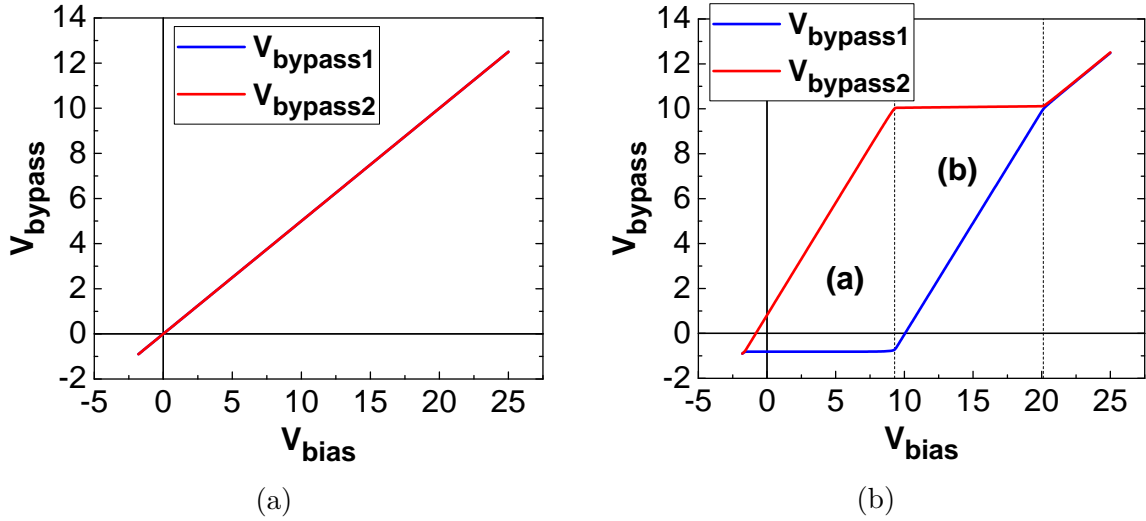


Figure 6-24:  $p$ -Si bypass diode currents: (a) at STC, and (b) with cell 9 shaded by 50 %.

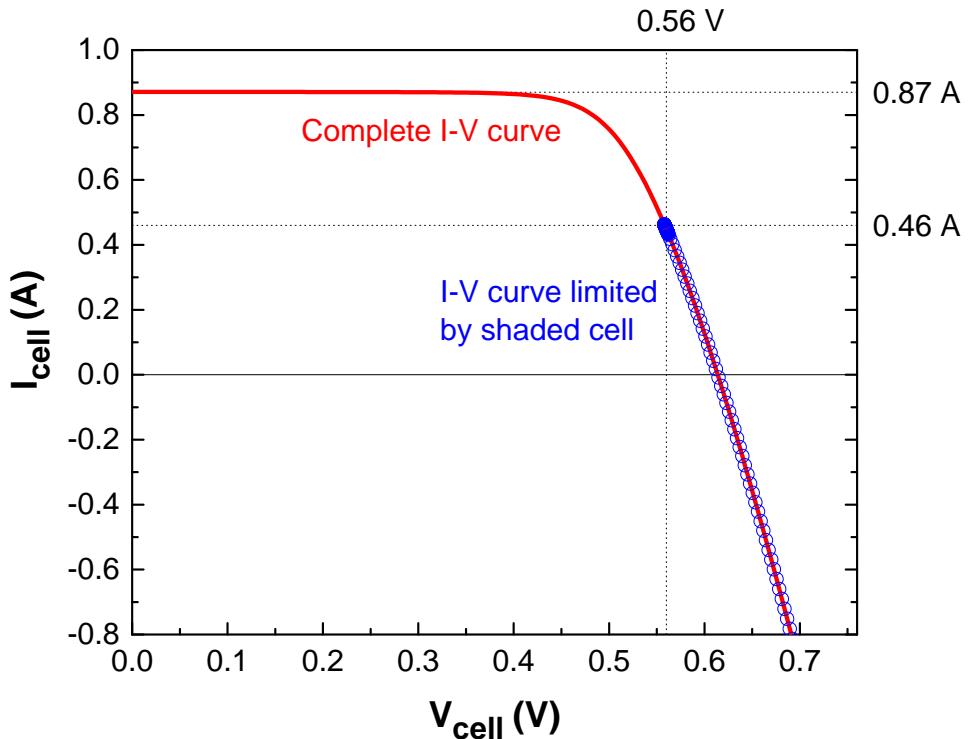


Figure 6-25: Illustration of the operating voltage constraint of non-shaded cells in a string containing a shaded cell.

The resulting mismatch in the short-circuit current between the cells in the string results in the shaded cell being reverse biased for most polarisations (except near the  $V_{\text{OC}}$ ), leading to power dissipation in the cell. At low-enough voltage bias values, the reverse bias becomes high enough to result in the activation of the bypass diode, fixing the voltage across it and across the contained string to around -0.7 V. Consider Fig. 6-24b at zero voltage bias. A voltage of -0.7 V is imposed on the affected string (string 1) by the activated bypass diode encompassing it. String 1 contains 17 cells functioning

at 0.56 V, resulting in the following balance:

$$17 \times 0.56V + V_{cell9} = -0.70V \quad (6.15)$$

$$V_{cell9} = -10.22V$$

imposing the operation point of the shaded cell. The number of cells per string can be chosen in this way to ensure the reverse bias does not exceed the cell breakdown voltage. At  $V_{OC}$ , the non-shaded string operates at:

$$V_{bypass2} = V_{bias} - V_{bypass1} \quad (6.16)$$

$$= +0.70V$$

resulting in each cell operating at  $0.70V / 18 = +0.039V$ .

In region (a) of Fig. 6-23b, as the voltage across the module increases, the string 1 (containing the shaded cell) stays at the same operating point with the voltage imposed by the bypass diode. The voltage across string 2 increases linearly. At a certain point (line separating regions (a) and (b)), the cells in string 2 operate at the same voltage as the non-shaded cells of string 1 (0.56 V). It is at this point that string 1 voltage starts increasing linearly, gradually turning off the bypass diode (see Fig. 6-23b). Region (b) is therefore characterised by an increase in string 1 voltage, which manifests itself in a reduction in the shaded cell reverse bias, while the string 2 stays at the same operating point. Region (b) ends at the point where the string 1 voltage reached the one of string 2, beyond which both strings increase linearly with applied voltage (in the same way as under STC conditions).

### 6.2.3.2 Study 2: Performance vs. Level of Shading

In the second study, a *p*-Si module was simulated under STC conditions, while the level of shading of a single cell (cell 9) was varied from 0 to 100% in 25% increments. The simulation was performed for the cases of zero and two bypass diodes (BPD) being installed. It was assumed that during a given module operation, a maximum power point tracking (MPPT) mechanism controlled the operating point to maximise the module power output.

Fig. 6-26 presents the simulation results - the PV module power output (above) and the shaded cell dissipated power (below) as a function of applied voltage bias. Solid lines represent the case of no BPD, while the dashed lines represent the case with BPD.

In the case of 0% shading, the module maximum power output is 11.0 W, which is evenly distributed among the 36 cells resulting in about 0.3 W of production per cell (not shown).

In the cases of 25 and 50% shading, the module power output drops to 10.0 and 7.1

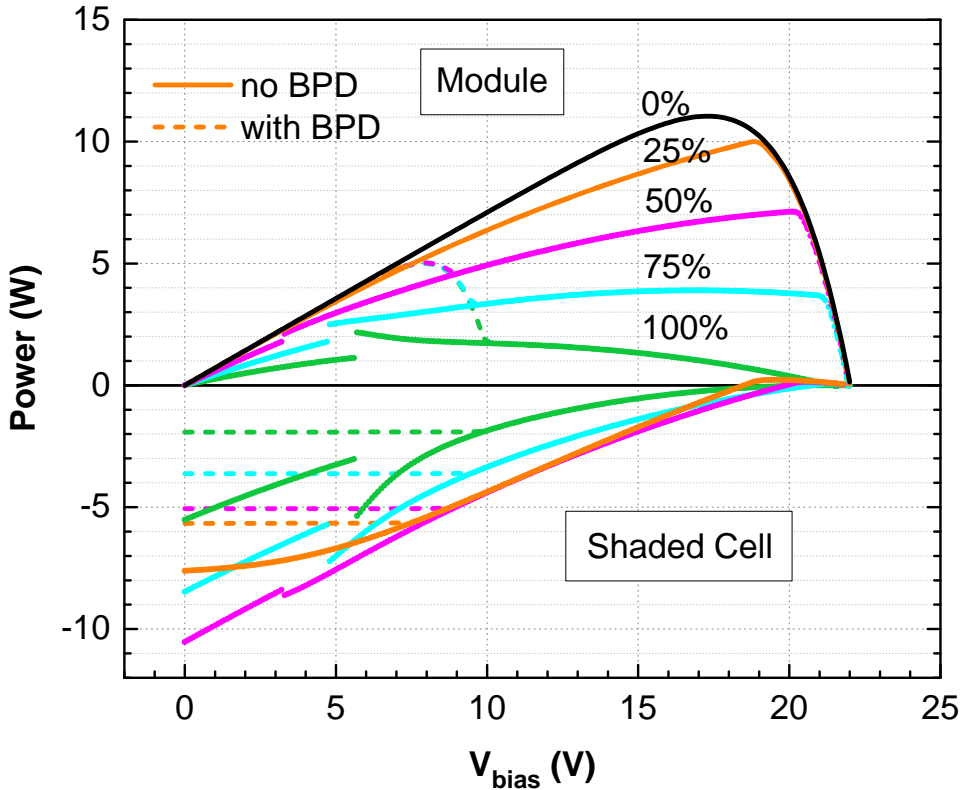


Figure 6-26:  $P$ - $V$  characteristics of module output power (above), and shaded cell dissipated power (below), for different levels of shading. The black line represents the case of no shading, while the orange, magenta, blue, and green lines represent the cases of 25, 50, 75, and 100% shading, respectively. The dissipated power values at low  $V_{bias}$  for shading rates of 50, 75, and 100% (magenta, blue, and green) disconnected segments in the range 0-6 V) are an artefact of Bishop's mathematical formulation of the cell-level avalanche current, which produces incorrect avalanche current values if  $V_{cell}$  values greater than  $V_{br}$  are imposed.

W, respectively, while the  $V_{MPP}$  (location of peak) shifts to the right. The associated shaded cell productions reduce to 0.2 and 0.1 W, respectively. In both shading cases, the addition of bypass diodes has no impact on performance. This is because the right-hand peak in module  $P_{MPP}$  remains higher than the BPD-resulting left-hand peak, meaning that the point of operation remains unchanged.

Consider the case of 75% shading and no BPD (blue solid lines). The module  $P_{MPP}$  drops to 3.9 W, and the  $V_{MPP}$  is 16.9 V, lower than in the previous shading cases. At this operating point, the shaded cell is reverse-biased and *absorbs* 0.8 W. The introduction of BPD in this case results in a left-hand peak in module  $P_{MPP}$  that is higher than the original right-hand peak. The operating point is therefore shifted to the  $V_{bias}$  corresponding to the left peak (i.e. a "turn-over" takes place), with two consequences:

- the module  $P_{MPP}$  is increased to 5.0 W (positive impact)
- the shaded cell power dissipation is increased to 3.6 W (negative impact)

Consider the case of 100% shading and no BPD (green solid lines). The module  $V_{MPP}$

is 5.7 V, much lower than in the case of 75% shading. The module power output is 2.2 W, while the shaded cell power dissipation is 5.4 W. Similarly to the previous case, the introduction of BPD results in a dominant peak which in this case shifts the operating point to the right. This has two consequences:

- the module  $P_{MPP}$  is increased to 5.0 W (positive impact)
- the shaded cell power dissipation is reduced to 1.9 W (positive impact)

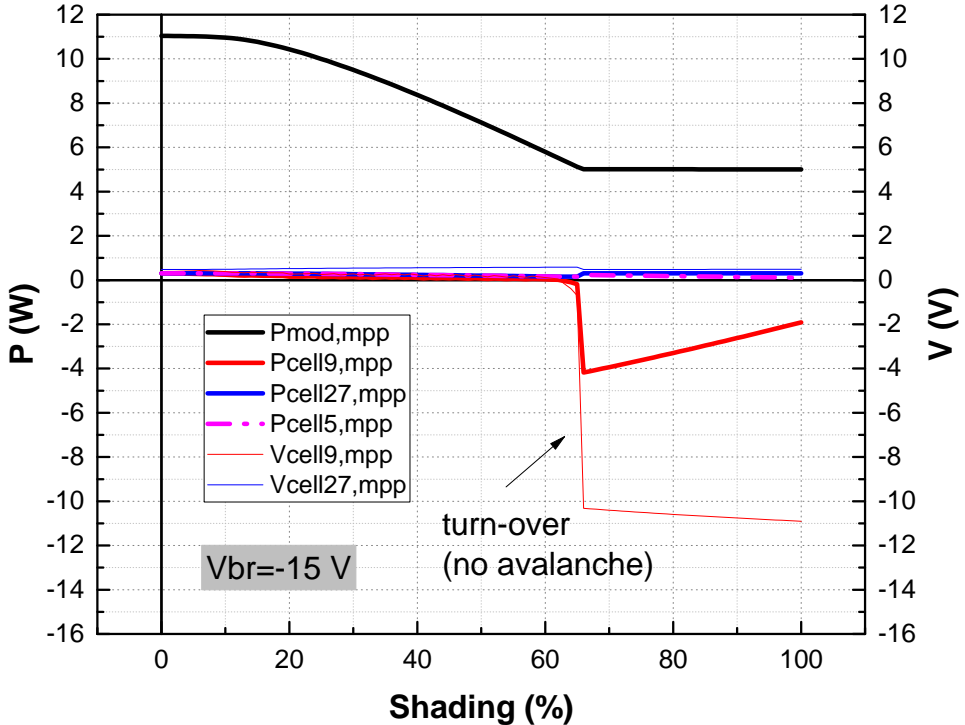
Comparing the results of these shading cases, it is evident that BPD serves the purpose of maximising production in partial shading conditions, while in certain cases negatively impacts the shaded cell dissipation. One can also note that in both "no BPD" and "with BPD" cases, there is a certain value of shading rate where a turn-over takes place due to a change in  $V_{MPP}$ . In the case "with BPD" the turn-over is expected between 50 and 75%, while in the case "no BPD" it should occur between 75 and 100%.

To examine the partial shading effect in more detail, the study was repeated for all shading rates of cell 9 (0 to 100% in 1% increments), and several electrical variables were evaluated at the voltage corresponding to the module  $P_{MPP}$ . Specifically, the variables saved were the power of the module, the power and voltage of the shaded cell (9), the power and voltage of the unshaded cell in the *unshaded* string (27), and the power of the unshaded cell in the *impacted* string (5). Figs. 6-27a and 6-27b show the results for the case of with and without BPD, respectively.

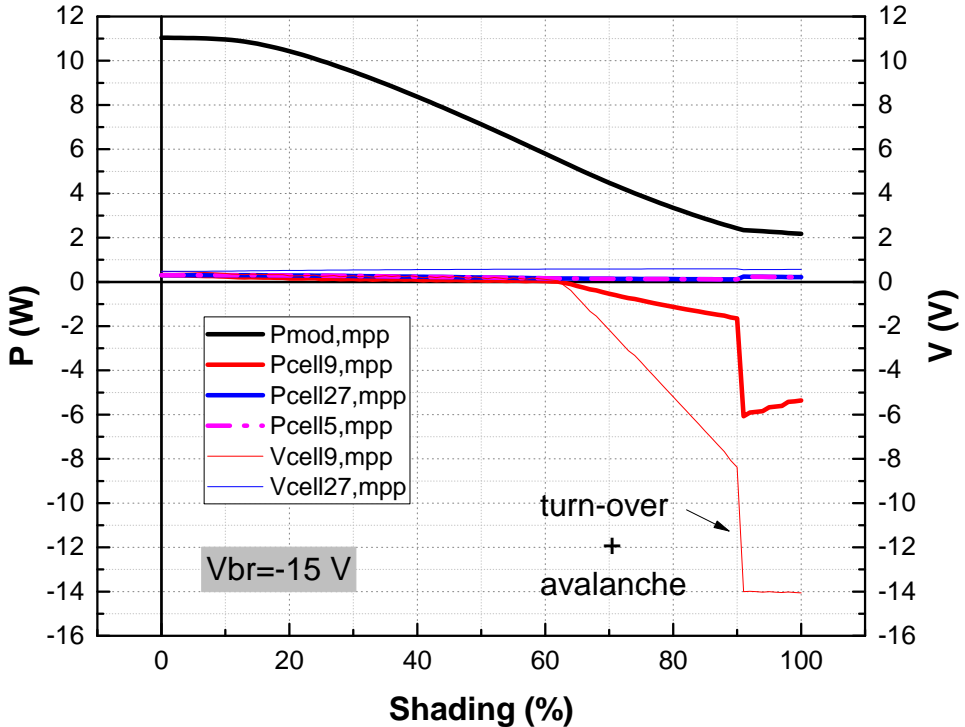
In both cases, as the shading is increased the module and shaded cell power outputs decrease. Equally, the shaded cell in both cases starts to dissipate power beyond a shading of 63% due to a negative cell voltage.

Consider now the case "with BPD" (Fig. 6-27a). At 65% shading, a turn-over occurs when the BPD turns on. The shaded cell voltage drops to -10.3 V, resulting in a power dissipation of 4.2 W. The cell voltage is not low enough to trigger an avalanche breakdown. As the shading is further increased, the module output power remains the same due to the BPD presence. The shaded cell's voltage continues to decrease slightly as it adapts to the imposed current. The shaded cell power dissipation decreases in magnitude since the cell current decreases faster than its voltage.

Fig. 6-27b presents the case of "no BPD". As the shading is increased beyond 63%, the module power output keeps decreasing. More importantly, the shaded cell voltage continues to decrease resulting in a growing dissipation. At 90% shading, a turn-over occurs since the module  $V_{MPP}$  is shifted to a lower polarisation (as it did in Fig. 6-26 when comparing the "75%" and "100%" cases). The turn-over results in the shaded cell voltage being low enough for it to abruptly enter the avalanche mode. The resulting power dissipation is about 6 W and in practice marks the end of the module's life. Therefore, the simulation results beyond the turn-over point have little practical value.



(a) Two bypass diodes



(b) No bypass diodes

Figure 6-27: Evolution of various electrical variables as a function of shading rate of a single PV cell (cell 9, in red) in a *p*-Si module otherwise submitted to STC conditions. Cell 5 (magenta) is a non-shaded cell in the same string as the shaded one. Cell 27 (blue) is a non-shaded cell in a string of non-shaded cells. In (a) the module is equipped with 2 bypass diodes, while in (b) no bypass diodes are installed.

Comparing the two graphs, the following conclusions can be made. The BPD turns on beyond a 65% shading, increasing the module power output compared to "no BPD". In the shading level range of 65 to 90%, the power dissipation in the shaded cell is higher if BPDs are used. Beyond 90% shading the BPDs prevent the avalanche breakdown from occurring. Overall, it is clear that the BPDs are of great importance for modules with many series-connected cells, boosting their production while keeping the cells safe from damage. The results of this study are coherent with results of Fertig et al. [139], who observed the same behaviour of cells and modules as a function of applied shading rate.

## 6.3 Discussion

Two approaches have been taken in modelling the electrical aspects of the system: empirical and equivalent circuit-based methods.

The Evans empirical model was chosen as the example of an empirical approach due to its simplicity and applicability to several PV technologies. It calculates the effective conversion efficiency and the power output using the average module irradiance and temperature as inputs. When coupled with the analytical model described previously, it proved accurate in describing the power production of frontal modules. The model excelled particularly in predicting power production at low irradiance levels. A disadvantage of this approach is that it assumes a uniform illumination of PV cells, while non-uniform module illuminations are not uncommon due to defined concentration zones and shadows. Calculating and using the average module flux with the Evans model gives way to the underestimation of shadows and similarly the overestimation of the reflector impact.

Due to the shortcomings of the empirical model, a equivalent circuit-based approach was employed to model the photoelectric effect. An *a*-Si:H cell was described with a single diode model, extended to include the phenomena of junction breakdown and *i*-layer recombination. A *p*-Si cell was similarly described with a double-diode model extended with the junction breakdown term. Modules were assembled with an electrical interconnection of cells, adding bypass diodes to the *p*-Si module. The advantage of the circuit-based approach is that it allows for producing complete  $I - V$  characteristics of the cells, including their behaviour under reverse-bias conditions. Furthermore, it allows the study of the influence of bypass diodes, which were shown to prevent junction breakdown in extreme partial shading conditions.

The use of the equivalent-circuit approach is the recommended approach in designing reflector-equipped systems, allowing one to study, anticipate, and design for electrical phenomena that could result in power losses or permanent damage cell damage.

# Chapter 7

## Calibration and Performance of EDStaR+SPICE

Before validating a given model's performance, it needs to be calibrated with a subset of measured data. The optical and electrical models should ideally be calibrated and validated *independently*. The optical model would use POA irradiance measurements as an input, while the electrical model would need both POA irradiance and operating temperature measurements. The experiment was equipped with temperature probes Pt-100, but *not* with POA irradiance sensors (at the time of writing). Therefore, the optical and electrical models could not be independently calibrated. The solution to this is to calibrate both models together as they work in conjunction to produce *I-V* curves, which can be compared to corresponding measurements. The use of measured operating temperature would isolate the uncertainty to that of the optical and electrical models.

Note that the parameters related to the reverse *I-V* characteristic, namely the Bishop parameters ( $a$ ,  $m$ , and  $V_{br}$ ), cannot be obtained through calibration since the measured *I-V* characteristics do not contain instances of junction breakdown. A sample cell was unavailable to perform the reverse characteristic measurement in the laboratory. Therefore, the Bishop parameters have been fixed to values found in the literature ( $a=0.1$ ,  $m=3.4$ ,  $V_{br_{a-Si}}=-15V$ ,  $V_{br_{p-Si}}=-20V$ ) [131, 132].

### 7.1 Calibration

The calibration of parameters must be done through trial and error since the governing equations are non-linear and transcendental. The model calibration therefore consists of varying the parameters until the experimental *I-V* curves are reproduced by the model. The model parameters to be estimated include optical and electrical parameters. The optical parameters to be estimated are:

- the reflector normal reflectance of direct irradiance (at zero angle of incidence)
- the reflector average reflectance of diffuse irradiance
- the PV module front glass normal transmittance of direct irradiance, and

- the PV module front glass average transmittance of diffuse irradiance.

Note that the obtained optical parameters represent *effective* values taking into account the spectral mismatch between the PV cell spectral response and the reflected or transmitted wavelengths. For this reason, the effective reflector properties are found for each PV technology. Similarly, the front glass transmittances must be evaluated independently for each technology due to the difference in their physical properties.

The electrical parameters to be estimated, common to both PV technologies, are  $J_0$ ,  $J_{SC,STC}$ ,  $R_s$ ,  $R_{sh}$ ,  $\alpha_{Isc}$ , and  $n$  (see Sec. 6.2). The *p*-Si electrical model has two additional parameters due to a second diode:  $J_{02}$  and  $n_2$ . The *a*-Si:H electrical model has three additional parameters due to the Merten term:  $d_i$ ,  $\mu\tau_{eff}$ , and  $V_{bi}$ .

Note that certain optical and electrical parameters can potentially compensate one another, as their influences on output current are in direct opposition. For example, a high transmittance coefficient of diffuse irradiance can perhaps be compensated by a lower value of  $J_{SC,STC}$ .

The calibration can be either be done by hand, or by an optimisation technique such as an evolutionary algorithm. Calibration by hand has the advantage of allowing a rapid estimation of parameters that give satisfactory results. An algorithmic approach may not have the advantage of intuition, but with enough time converges to the optimal parameter set (minimising a chosen cost function).

A "teaching-learning based optimisation" (TLBO) algorithm [140] has been developed for the purpose of systematic calibration. It is a general purpose evolutionary algorithm which features easy implementation, good performance (e.g. fast convergence) and robustness (e.g. good resistance to local minimum traps). Furthermore, it allows for a large search space for each parameter without the need to provide an initial estimate of the result. TLBO was modified in two ways compared to the article:

- multiple *I-V* curves were used as inputs (along with the corresponding transmitted irradiance and operating temperature data), instead of a single one
- the cost function in the article (see (7.1)) was adapted to give a higher weight to *I-V* points with a higher power (see (7.2)). This was done to ensure a good fit of  $P_{MPP}$ .

$$F(X) = \frac{\sum_{k=1}^p \left\{ \left[ I^{exp}(V_k) - I^{cal}(V_k, X) \right]^2 \right\}}{p} \quad (7.1)$$

$$F(X) = \frac{\sum_{k=1}^p \left\{ \left[ I^{exp}(V_k) - I^{cal}(V_k, X) \right]^2 I^{exp}(V_k) V_k \right\}}{p} \quad (7.2)$$

where  $X$  represents a given parameter set,  $k$  is the index of a given *I-V* point,  $p$  is the total number of points in a given *I-V* curve, and  $V_k$  is the voltage at point  $k$ .

The input data consisted of many  $I$ - $V$  curves, representing the targeted model output, and their respective operating temperature, BNI, and DHI measurements. Specifically, a total of 200  $I$ - $V$  curves was sampled from ten consecutive days: 17th to 26th of May, 2014. The set contained both clear and cloudy days. The associated daily average diffuse fractions are 0.26, 0.34, 0.25, 0.89, 0.98, 0.68, 0.85, 0.81, 0.70, and 0.89.

The electrical parameters for  $p$ -Si and  $a$ -Si:H cells obtained through calibration are outlined in Table 7.1. These parameters correspond to modules 16 and 15, respectively.

Table 7.1: Electrical parameters of  $p$ -Si and  $a$ -Si:H cells corresponding to modules 16 and 15, respectively

Parameter	$p$ -Si	$a$ -Si:H
$Area (cm^2)$	22.0	65.9
$J_0 (A/cm^2)$	$4.44 \times 10^{-12}$	$8.24 \times 10^{-19}$
$J_{02} (A/cm^2)$	$1.00 \times 10^{-8}$	—
$J_{SC,STC} (A/cm^2)$	$3.96 \times 10^{-2}$	$8.66 \times 10^{-3}$
$Rs (\Omega.cm^2)$	0.932	33.0
$Rsh (\Omega.cm^2)$	$6.70 \times 10^3$	$6.36 \times 10^5$
$\alpha_{Isc} (1/^\circ C)$	$1.041 \times 10^{-3}$	$1.00 \times 10^{-3}$
$n_1$	1.00	1.70
$n_2$	1.819	—
$a$	0.1	0.1
$m$	3.4	3.4
$V_{br} (V)$	-15.0	-20.0
$d_i (cm)$	—	$3.46 \times 10^{-5}$
$\mu\tau_{eff} (cm^2/V)$	—	$1.00 \times 10^{-8}$
$V_{bi} (V)$	—	1.80

The thermal model (discussed in the next chapter) has been then calibrated with the calculated irradiances. The subset used for the calibration of the thermal model is 15th May - 31 December, 2014.

## 7.2 Validation

The performance of the combined model is demonstrated on three levels:

1. individual  $I$ - $V$  curves
2. daily production profile ( $P_{MPP}$  comparison)
3. annual production profile (output power integrated daily)

Figure 7-1 presents the first level comparison for module 6 on May 17th, 2014, a relatively clear day. The  $I$ - $V$  curves are rather well reproduced throughout the day, especially near the  $P_{MPP}$ . As the cost function of the calibration is weighted to favour accuracy near the  $P_{MPP}$  at the expense of the accuracy near  $I_{SC}$  and  $V_{OC}$ , the resulting modelled curves sometimes overestimate the  $I_{SC}$  (for example at 12:05), or underestimate the  $V_{OC}$  (for example at 06:24).

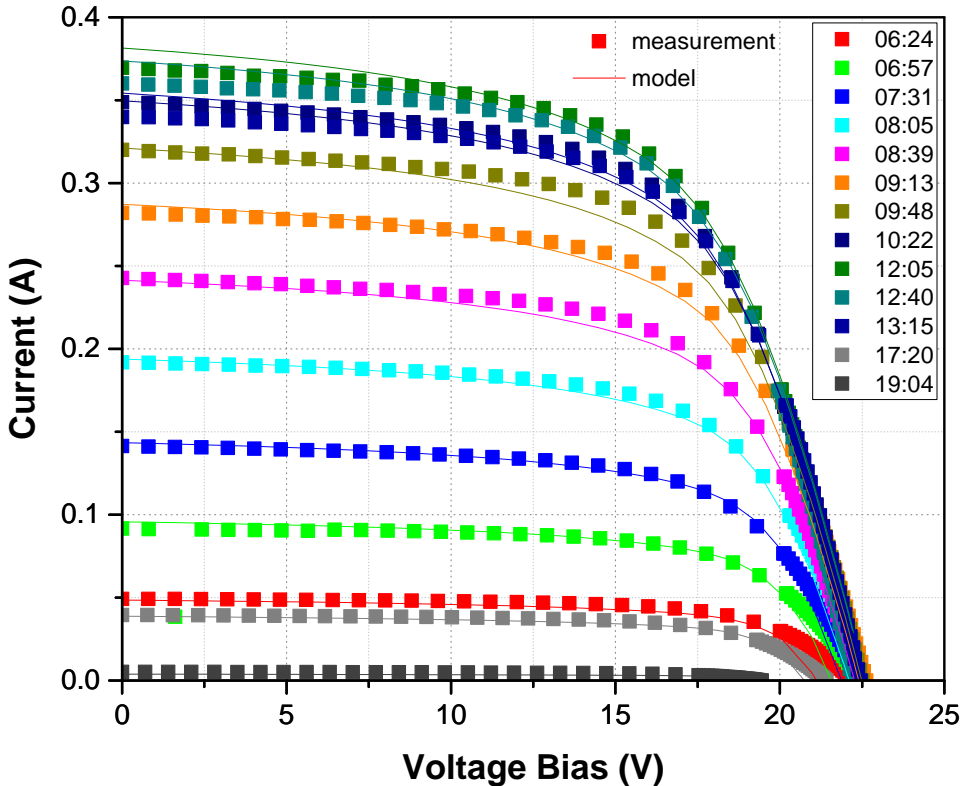


Figure 7-1: Comparison of experimental and numerical  $I$ - $V$  curves for module 6 on May 17th, 2014, after a calibration of model parameters. The calibration was performed using 200  $I$ - $V$  curves sampled from 10 consecutive days in May, 2014.

Figure 7-2 presents the experimental and numerical daily production profiles of six modules: frontal, edge and non-edge modules of both  $a$ -Si:H and  $p$ -Si technologies on May 17th, 2014. The performance of all six modules has been successfully reproduced. Due to the advantages of both the optical and electrical models, the edge effect on production has been successfully reproduced for both technologies as seen in the magenta and black curves.

Figure 7-3 presents the experimental and numerical long term production profiles, integrated daily, for four representative modules: 6, 15, 5, and 16. The temporal range of the  $I$ - $V$  and temperature measurement subset used for the calibration of optical and electrical models is highlighted in blue (17th - 26th May, 2014). EDStaR+SPICE was used with appropriate inputs, including the measured operating temperature, to reproduce the daily produced energy until the rest of the year.

The thermal model ETM (discussed in the next chapter) has been then calibrated with the calculated irradiances with the subset of 15th May - 31 December, 2014, highlighted in yellow. The complete model (EDStaR+SPICE+ETM) has been used to reproduce measurements from 1st January, 2015 to 31st August, 2016.

Note that there is a significant amount of holes in the graph, represented by the connecting lines spanning several days. This is due to the absence or the bad quality of

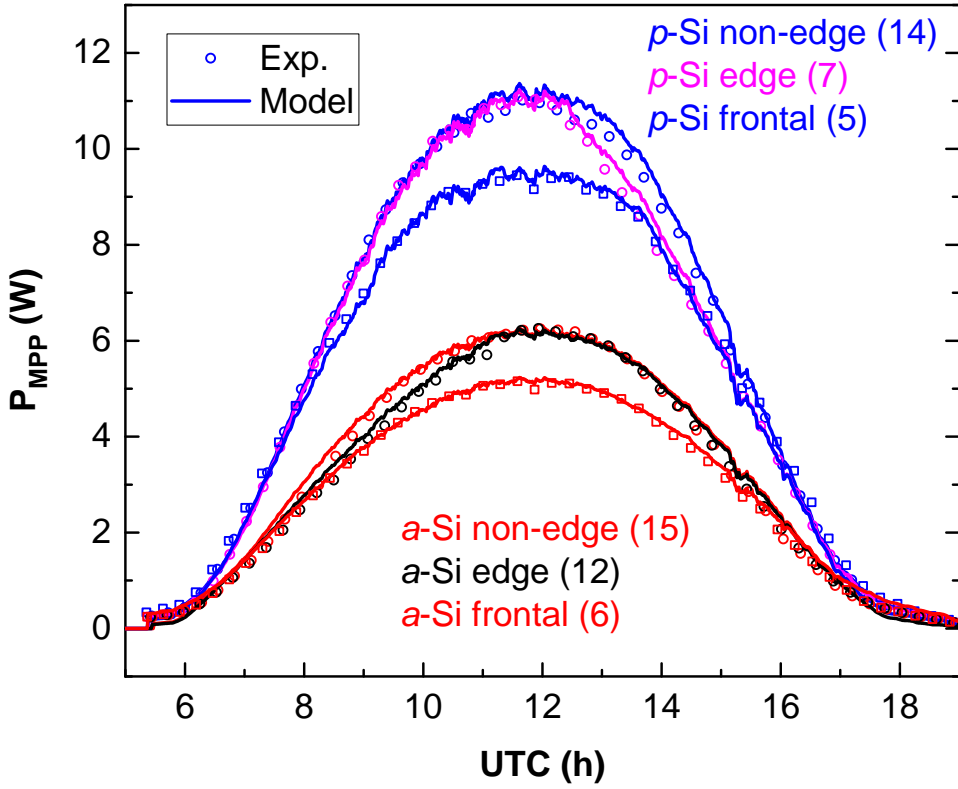


Figure 7-2: Comparison of experimental and numerical daily production profiles for frontal modules (5 and 6), edge modules (7 and 12) and non-edge modules (14 and 15), on May 17th, 2014.

one or more key inputs -  $I$ - $V$  characteristic, module temperature, BNI or DHI - in which case the model was not executed and the corresponding measurement is not shown. As seen in the figure, the model shows a good performance in predicting the power output of modules 6, 15, and 5, and 16. The relative errors for modules 6, 15, 5, and 16 are -2.0%, +1.9%, -4.4% and -4.5%, respectively. The biggest discrepancies between experimental and numerical values come from measurement errors during days with an intermittent solar resource. With the same training period, the model seems more accurate for  $a$ -Si:H modules. This is likely due to the lower uncertainty related to the electrical model of the  $a$ -Si:H module. For instance, there are no bypass diodes to model, and the mismatch conditions are much less frequent and severe. Note that a longer training period could further decrease the prediction error of the model.

Figures 7-4 and 7-5 present a direct comparison of experimental and numerical  $P_{MPP}$  used to compute the daily integrals in Fig. 7-3. A good performance is observed for all four representative modules (frontal and reflector-equipped  $a$ -Si:H and  $p$ -Si), with RMSE ranging from 0.43 to 0.87 W. Note the two clouds of outliers in each of the four graphs, where the model seems to severely over- and under-estimate the module power output. This is due to the previously-mentioned error in the  $I$ - $V$  curve measurement timestamp, caused by sequentially measuring the 18 modules and saving a single timestamp at the

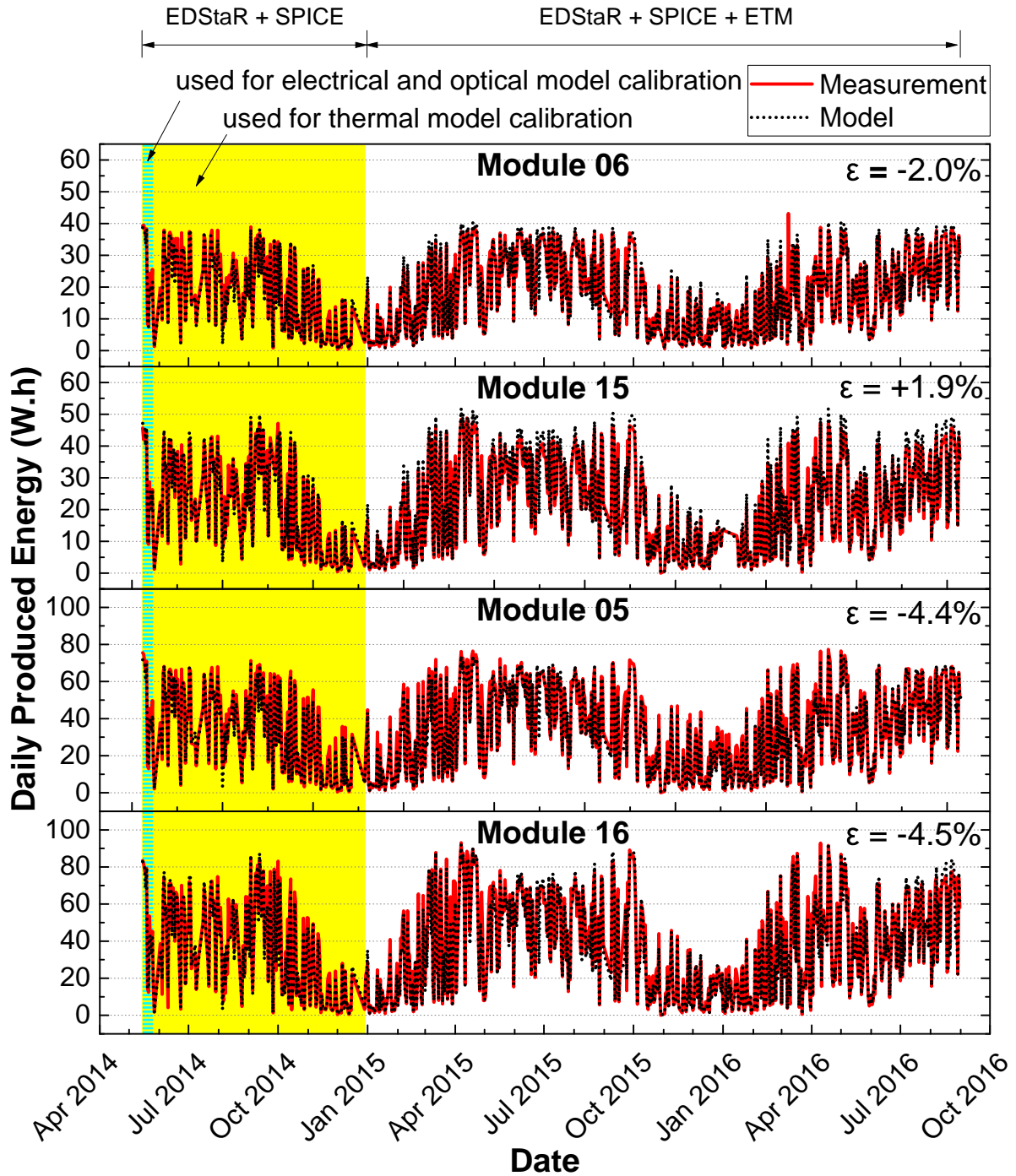


Figure 7-3: Comparison of experimental and numerical values of the annual distribution of the daily produced energy for modules 6, 15, 5, and 16, for the period of 15th May to 31st December, 2014. The temporal range of the  $I-V$  and temperature measurement subset used for the calibration of optical and electrical models is highlighted in blue (17th - 26th May, 2014). The subset used for the calibration of the thermal model (discussed in the next chapter) is highlighted in yellow (15th May - 31 December, 2014).  $\epsilon$  represents the relative difference between the modelled and measured total produced energy (over the range 15th May, 2014 - 31st August, 2016).

end. In highly variable irradiance conditions, several minutes of timestamp error can

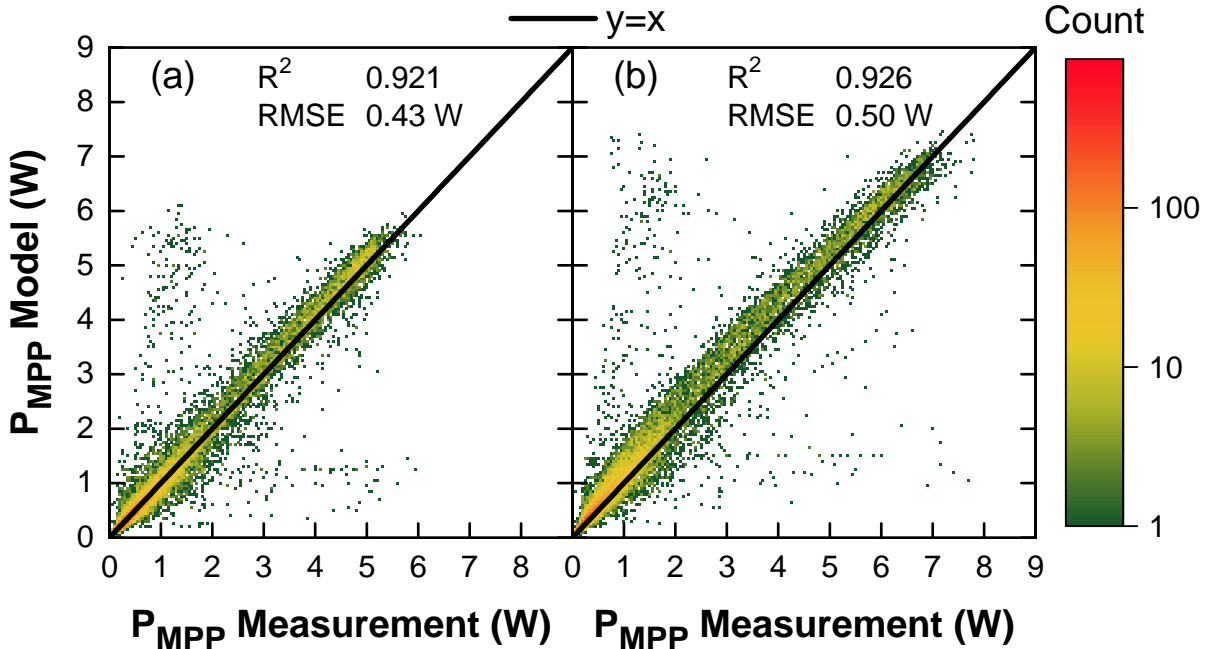


Figure 7-4: Comparison of experimental and numerical  $P_{MPP}$  values for (a) module 6 (frontal  $a\text{-Si:H}$ ), and (b) module 15 (row 3  $a\text{-Si:H}$ ), for the period of 15th May to 31st August, 2016. The clouds of points far from the diagonal correspond to points with erroneous timestamps taken during periods of variable solar resource. Filter based on irradiance fluctuations was already applied and eliminated most of the points in the clouds. Stricter filters on irradiance fluctuations would be necessary to eliminate these points.

result in it being associated with much different surface irradiance values, resulting in errors. The positive or negative bias at lower  $P_{MPP}$  values (0-2 W for  $a\text{-Si:H}$ , 0-4 W for  $p\text{-Si}$ ) is due to suboptimal optical parameters concerning diffuse irradiance. As the cost function has been weighted to favour higher  $P_{MPP}$  over lower ones, the  $I\text{-}V$  curves associated with diffuse irradiance have been by default given less importance. The larger spread in this area is partly due to the timestamp issue, and partly due to the uniform-sky assumption. If the diffuse irradiance source had been modelled in more detail (e.g. taking into account the position of the Sun), a lower spread could have perhaps been achieved in this region.

### 7.3 Conclusion

As seen in this chapter, the combined EDStaR+SPICE model shows a good performance in reproducing experimental  $I\text{-}V$  curves. The model's robustness is demonstrated by its ability to reproduce complete daily production profiles of modules of both technologies, situated in different positions compared to the reflector. Finally, with a learning dataset of just ten days in May, the model succeeded in reproducing the daily electricity production until the end of the year with the measured module temperatures. After a calibration

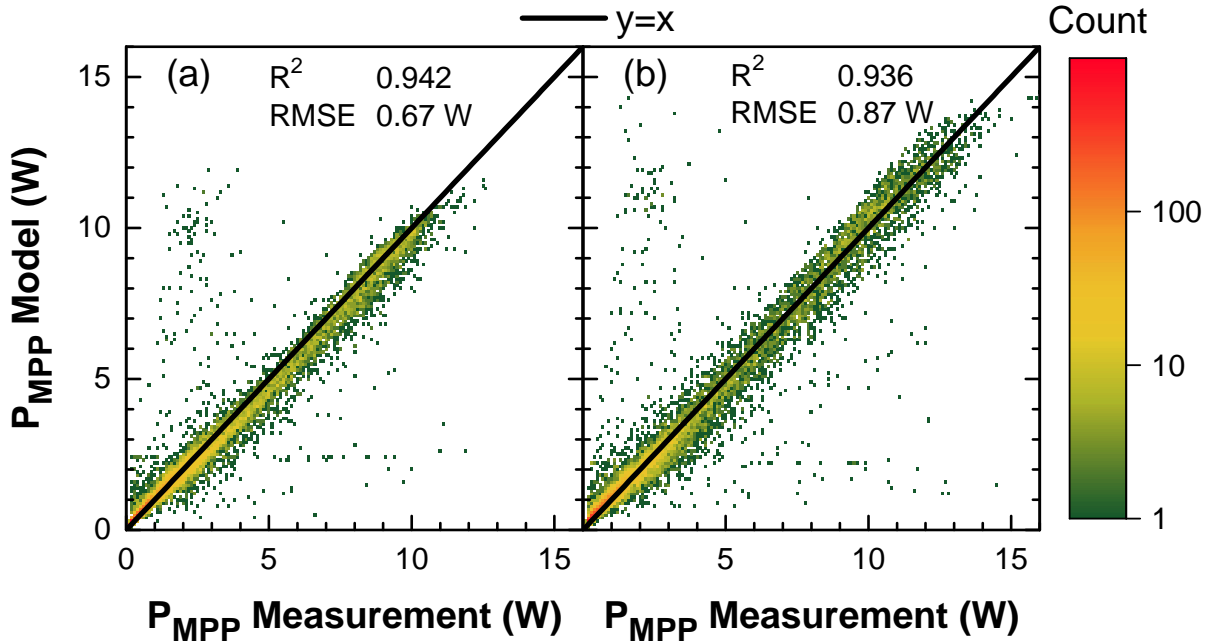


Figure 7-5: Comparison of experimental and numerical  $P_{MPP}$  values for (a) module 5 (frontal p-Si), and (b) module 16 (row 3 p-Si), for the period of 15th May to 31st August, 2016. The clouds of points far from the diagonal correspond to points with erroneous timestamps taken during periods of variable solar resource. Filter based on irradiance fluctuations was already applied and eliminated most of the points in the clouds. Stricter filters on irradiance fluctuations would be necessary to eliminate these points.

of the thermal model with about a half a year of measurements, the combined model was able to reproduce over two years of power output, purely based on radiative and environmental variables (i.e. the operating temperature was calculated).

The next chapter details the proposed thermal model able to reproduce the temperature measurements as a function of calculated module irradiances (through SIRTA-measured BNI and DHI) and measured environmental variables (e.g. ambient temperature and wind speed).

# Chapter 8

## Thermal Modelling

As seen before, the PV cell performance decreases with increasing operating temperature, owing to increased rates of internal carrier recombination caused by increased carrier concentrations. Therefore, an accurate prediction of the PV module performance requires the knowledge (or estimate) of the PV cell operating temperature. Various thermal models exist for predicting the operating temperature, involving basic environmental variables and numerical parameters that are material or system dependent. All of them rely on representing different mechanisms of heat transfer contributing to the final temperature. This chapter presents the thermal modelling performed as a part of the thesis.

### 8.1 State of The Art

Most of the models proposed in the literature are empirical, meaning that the proposed equations were fitted through a large number of data to yield empirically-derived, system-specific coefficients [74, 102, 128, 129, 141–159].

The most commonly used empirical models (such as the ones proposed by King [141] and Faiman [142]) are instantaneous in nature, meaning that the thermal mass of the PV cells is considered negligible. The consequence of this assumption is that the operating temperature can be 1) severely overestimated during spikes of high irradiance in cloudy periods, and 2) severely underestimated during cloud passages in clear periods. In these scenarios, the change in temperature is assumed instantaneous, while it is in fact gradual and asymptotical in nature.

King et al. [141] (Sandia Labs) propose the following correlation for the module temperature:

$$T_M = T_{amb} + E \times \exp(a + b \times WS) \quad (8.1)$$

where  $T_M$  is the back-surface module temperature ( $^{\circ}\text{C}$ ),  $T_{amb}$  is the ambient air temperature ( $^{\circ}\text{C}$ ),  $E$  is the global solar irradiance incident on the module surface ( $\text{W}/\text{m}^2$ ),  $WS$  is the wind speed measured at 10-m height ( $\text{m}/\text{s}$ ), and  $a$  and  $b$  are empirically-determined coefficients. In the above equation,  $a$  establishes the upper limit for module temperature

at zero-wind conditions, for example due to natural convection-driven heat losses. The parameter  $b$  represents the rate at which module temperature drops as wind speed increases. The reported RMSE is 5 °C, resulting in a 3% uncertainty in the module power output.

Note that the King model works with incident, rather than transmitted irradiances. This may lead to overestimations at high incidence angles, where a part of the flux is reflected away from the module and does not contribute to heating the modules. Furthermore, the amount of heating is related to the PV cell conversion efficiency, which is not explicitly taken into account by King. As the photons that contributed to the creation of electron-hole pairs are considered to have not heated the cell, the amount of heating is inversely proportional to the conversion efficiency. Wind direction was reported to have a small but noticeable impact on operating temperature, and was finally not included in their model. They also observed a degradation in model performance due to thermal transients caused by the module's heat capacitance, which is inevitable for instantaneous models.

Faiman proposed a more comprehensive correlation, overcoming some of the limitations of the King model:

$$T_M = T_{amb} + \frac{E(\eta_o - \eta_e)}{U_0 + U_1 \times WS} \quad (8.2)$$

where  $T_M$  is the back-surface module temperature (°C),  $T_{amb}$  is the ambient air temperature (°C),  $E$  is the global solar irradiance incident on the module surface (W/m<sup>2</sup>),  $WS$  is the wind speed measured at 10-m height (m/s),  $\eta_o$  is the optical efficiency (measurement of optical losses),  $\eta_e$  is the conversion efficiency, and  $U_0$  and  $U_1$  are empirically-determined heat loss coefficients similar to  $a$  and  $b$  in the King model. Note that Faiman considers a constant conversion efficiency, while it in fact varies with temperature. Nevertheless, the model showed a good performance, resulting in a RMSE of 1.85 K. This error was reported to result in 1% uncertainty in power output.

Faiman [142] has measured nighttime inter-cell temperature differences within a given module of up to 0.26 K (RMSE), the difference being non-systematic across the 7 modules tested. The daytime measurements showed that central cells were on average 2 K hotter than corner cells. This information gives an idea of a good empirical model performance, which by definition assumes a uniform temperature across the cells.

There are examples of dynamical empirical models [145, 148, 150, 152, 154, 155], which attempt to represent the PV cell thermal mass to produce a more accurate prediction. This is often done by employing an energy balance approach taking into consideration various heat transfer mechanisms (including radiative), and often using one or more past measurements/results to estimate the current operating temperature.

Several authors propose a time-dependent physics-based thermal model, using a dis-

cretised domain (2-D or 3-D) and applying fundamental laws of physics and numerical methods to model the relevant heat transfers [160–170]. This is of particular importance when heat sinks are relied upon to divert heat (e.g. in HCPV applications), or when natural convection is of particular importance to cool the modules [165–167, 169, 171] (e.g. in building-integrated PV applications). Such models are more computationally-intensive than empirical models, and are therefore rarely included in commercial PV array modelling software such as PVsyst.

## 8.2 Empirical Thermal Model (ETM)

As a first approach to modelling the operating temperature, an instantaneous empirical model was developed, inspired by the Sandia model [141]:

$$T_M = T_{amb} + (C_0 \times E_B + C_1 \times E_D) \times \exp(C_2 \times WS) \quad (8.3)$$

Compared to the Sandia model, the contribution of direct and diffuse irradiances was separated to reflect the difference in spectral compositions of the two. This is of particular importance since the reflector often results in different concentrations of direct and diffuse irradiances. Furthermore, the parameter  $a$  in the Sandia model was removed as limited natural convection-driven heat-losses are expected (the modules are a part of a closed triangular cavity).

As can be seen in Fig. 8-1, the model shows a good performance over the entire range of measurements. The RMSE is below 5 °C for all four modules, which is the same order of magnitude as the original Sandia model. The parameter  $C_2$ , corresponding to parameter  $b$  in the Sandia model, is consistent with values obtained by King.  $C_2$  was found to vary from -0.0706 to -0.1056, while  $b$  was reported by King to vary from -0.0455 to -0.130.

For all modules analysed,  $C_1$  has been found to be about 2.5 times greater than  $C_0$ . This means that a Watt of diffuse irradiance heats the PV cells about 2.5 times more than a Watt of beam irradiance. This difference is explained by the difference in the spectral distributions of the two irradiances, since the diffuse irradiance contains a larger fraction of short-wavelength photons.

Furthermore, the similarities and differences in parameter values across different modules are coherent and explainable. Parameters  $C_0$  and  $C_1$  are coherent for modules with a unique PV module technology, which is a result of a unique module front glass and PV cell spectral response.  $C_0$  and  $C_1$  of  $p$ -Si modules are higher than  $a$ -Si:H modules, which is consistent with the conclusions made in Sec. 3.3.

At the same time, the wind speed coefficient,  $C_2$ , is shared by modules of the same row. As wind has a better access to the row 3 modules compared to those of row 1, these

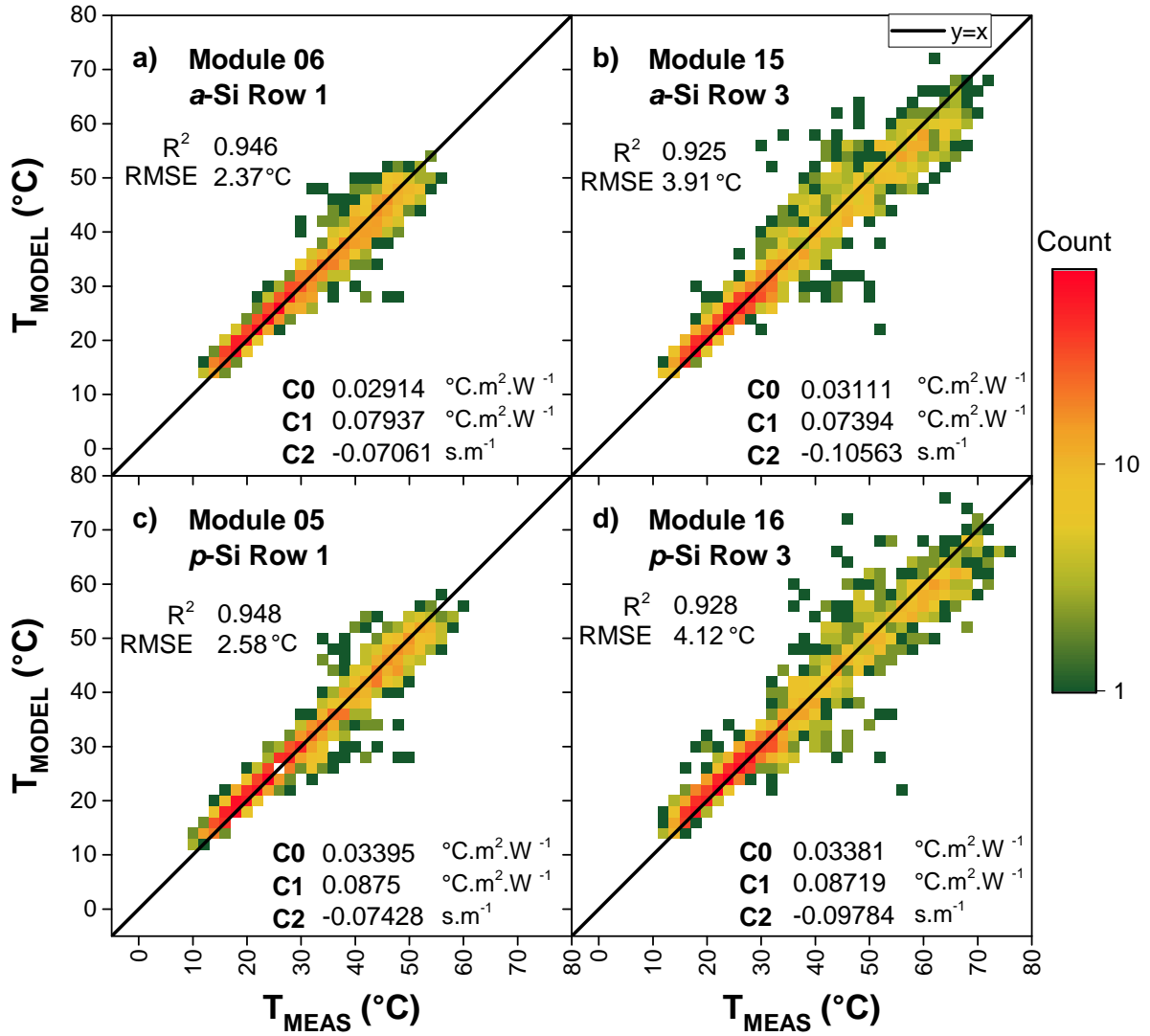


Figure 8-1: Performance of the proposed empirical model, fitted for a) a Row 1 *a*-Si:H module (# 06), b) a Row 3 *a*-Si:H module (# 15), c) a Row 1 *p*-Si module (# 05), and d) a Row 3 *p*-Si module (# 16). The period considered was 15th May - 31st December, 2014.

modules are cooled more per unit of wind speed. This results in a higher (more negative) value of  $C_2$  for row 3 modules compared to row 1 modules.

### 8.3 Discussion

An empirical operating temperature model was developed in the scope of this thesis, which was an adaptation of the well-known King model. The model calculates the cell operating temperature as a function of instantaneous values of ambient temperature, direct and diffuse plane-of-array irradiances, and wind speed. After calibration, the model performed with an RMSE smaller than 5 °C for all modules. This accuracy results in an error in power production smaller than 3 %, which is acceptable for most purposes.

The accuracy and the obtained coefficients are consistent with the values found in King's paper [141]. The coefficients obtained through calibration show that diffuse irradiance heats the cells about 2.5 times more than direct irradiance, owing to spectral effects. Nevertheless, direct irradiance is in most cases expected to be the dominant source of heat in absolute terms.

Due to a lack of time, Faiman's model was not tested for performance, but should be explored in future works due to the higher performance reported in the paper ( $\text{RMSE} < 2 \text{ }^{\circ}\text{C}$ ).

A physics-based, fluid dynamics model was not developed due to the sufficient accuracy of the proposed empirical model. Nevertheless, it could be used to achieve a better model accuracy by more precisely describing the thermal exchanges. For example, when the irradiance increases rapidly, the heat capacity of the modules allows it to remain cool for a certain time, reducing the rate at which efficiency decreases. This effect cannot be explained by the proposed empirical model.

Despite this potential, the development and calibration of such a model would be challenging due to:

- poor availability of bibliographic references for open, differentially-heated triangular cavities with (likely) turbulent interior flow conditions
- lack of sufficient temperature and air velocity sensors inside the cavity

A comprehensive study of the thermal exchanges inside the cavity is therefore left as a perspective.

THIS PAGE INTENTIONALLY LEFT BLANK